Third reply to the Editor´s comments

We would like to thank the Editor for his comments which we have addressed below. We keep the editor´s comments in red font and our replies in black font.

Dear authors,

Thank you for the clarifications and corrections. I would like to ask you some minor corrections.

As it stands, the phrase "Note that we convert per meg to parts per million equivalent by multiplying per meg by
0.209500 (the O2 mole fraction of atmospheric air) (Machta and Hughes, 1970)." is still incorrect or misleading at least. (Please also note that the title of the Machta and Hughes paper in the reference list contains a typographical error.)

The typo is now corrected to Atmospheric

First, parts "per million equivalent" seems to be science slang and the phrase should be rewritten as to explain the conversion between the measurement quantities "mole fraction" (commonly expressed in micromole/mole or ppm) and delta (commonly given in per meg units). Just talking about unit conversion could be misleading as the quantities that are converted into each other are completely different (we are not talking about conversion from inch to cm, for example).

We have now changed to sentence:
“Note that we convert per meg to parts per million equivalent by multiplying per meg by 0.209500 (the O2 mole fraction of atmospheric air).”

to

“Note that under the assumption that the atmospheric N2 content is constant (i.e. N2sample equals N2reference), we convert relative changes in oxygen given in per meg following equation 1 to oxygen changes in parts per million (equivalent to micromol/mol) by multiplying by the O2 mole fraction (O2reference) expressed as 209500 ppm. Hence 1 ppm corresponds roughly to 4.8 per meg, or 1 per meg to 1/4.8 (209500/10^6) ppm.”

Second, the conversion factor is correct if we are concerned with relative changes, ie if delta changes by 1 per meg, then the O2 mole fraction changes by 0.2095 ppm. However, readers not familiar with O2 measurements or the delta notation will understand the sentence as 1 per meg corresponding to 0.2095 ppm and, correspondingly, that the mole fraction of O2 in air of ~ 0.2095 (or 209500 ppm) must correspond to 209500 per meg, which is obviously wrong. Since your article uses both quantities (mole fractions as well as delta values), the definition of quantities and units as well as the conversion formula should be given, preferably based on physical quantities with SI units. Note that AMT is a specialised journal dedicated to measurement techniques. Therefore, the correct definition of measurement quantities and their units is central and cannot be neglected.

See the comments above

Third, it is absolutely not trivial how the CRDS technology can measure delta (or O2/N2), because N2 is not measured (by that technology). The same holds for the mole fraction (O2/air). This is another reason why the measurand (absorption of O2) and its relation to the O2 mole fraction or the delta(O2/N2) should be clearly defined in the manuscript. Please explain the measurement process in more detail (what is measured, what is obtained from calibration and how).
Please understand that all this information must be given before the paper can be published.

The editor is correct that the instrument presented here measures the O2 mole fraction only. How the O2 concentration is obtained is clearly stated in the manuscript in chapter 2 followed by discussions on dependencies of the O2 mole fraction that have been thoroughly investigated as described for instance in lines 311 to 319.

High-precision atmospheric oxygen measurement comparisons between a newly built CRDS analyzer and existing measurement techniques

Tesfaye A. Berhanu[1,2], John Hoffnagle[2], Chris Rella[2], David Kimhak[2], Peter Nyfeler[1], Markus Leuenberger[1]

[1]*Climate and Environmental Physics, Physics Institute and Oeschger Centre for Climate Change Research, University of Bern, Bern, Switzerland*

[2]*Picarro Inc., 3105 Patrick Henry Drive, Santa Clara, CA, USA*

Abstract

Carbon dioxide and oxygen are tightly coupled in land-biospheres CO_2 - O_2 exchange processes, while they are not coupled in oceanic exchange. For this reason, atmospheric oxygen measurements can be used to constrain the global carbon cycle, especially oceanic uptake. However, accurately quantifying the small (~1-100 ppm) variations in O_2 is analytically challenging due to the very large atmospheric background which constitutes about 20.9 % (~209500 ppm) of atmospheric air. Here we present a detailed description of the analyzer and its operating principles as well as comprehensive laboratory and field studies for a newly developed high-precision oxygen mixing ratio and isotopic composition analyzer (Picarro G-2207) that is based on cavity ring-down spectroscopy (CRDS). From the laboratory tests, we have calculated a short-term precision (standard error of one-minute O_2 mixing ratio measurements) of < 1 ppm for this analyzer based on measurements of eight standard gases analyzed for two hours consecutively. In contrast to the currently existing techniques, the instrument has an excellent long-term stability and therefore a calibration every 12 hours is sufficient to get an overall uncertainty of < 5 ppm. Measurements of

ambient air were also conducted at the High-Altitude Research Station, Jungfraujoch and the Beromünster tall tower in Switzerland. At both sites, we observed opposing and diurnally varying CO_2 and O_2 profiles due to different processes such as combustion, photosynthesis and respiration. Based on the combined measurements at Beromünster tower, we determined height dependent O_2:CO_2 oxidation ratios varying between -0.98 to -1.60 , which increase with the height of the tower inlet, possibly due to different source contribution such as natural gas combustion with high oxidation ratio and biological processes which are at the lower end.

1. Introduction

Atmospheric oxygen comprises about 20.9 % of the global atmosphere and in the past decade its concentration decreased at a rate of ~ 20 per meg yr^{-1} (Keeling and Manning, 2014) mainly associated with the increase in fossil fuel combustion. Measurements of atmospheric O_2 are reported as the ratio to the N_2 concentration and expressed as $\delta(O_2/N_2)$ because the variations in the concentrations of other atmospheric gases such as CO_2 can influence the O_2 partial pressure while this ratio is insensitive to these changes in other gases. Atmospheric O_2 is commonly expressed in units of per meg due to its small variability with respect to a large background, where

$$\delta\left(\frac{O_2}{N_2}\right)(per\ meg) = \left(\frac{(\frac{O_2}{N_2})_{sample}}{(\frac{O_2}{N_2})_{reference}} - 1\right).10^6 \qquad (1)$$

Note that under the assumption the atmospheric N_2 content is constant (i.e. $N_{2sample}$ equals $N_{2reference}$), we convert relative changes in oxygen given in per meg following equation 1 to oxygen changes in parts per million (equivalent to micromol/mol) by multiplying by the O_2 mole fraction ($O_{2reference}$) expressed as 209500 ppm. ~~Note that we convert per meg to parts per million equivalent by multiplying per meg by 0.209500~~ (the O_2 mole fraction of atmo~~ps~~spheric air) (Machta and Hughes, 1970). Hence 1 ppm corresponds approximately to

4.8 per meg, or 1 per meg to 1/4.8 (209500/10^6) ppm

In contrast to O_2, the global average atmospheric CO_2 mixing ratio increased to 405.0 ppm averaged over 2017 since its preindustrial value of 280 ppm (Le Quéré et al., 2017). As the variability of atmospheric oxygen is directly linked to the carbon cycle, both its short and long-term observations can be used to better constrain the carbon cycle. For example, since first suggested by Keeling and Shertz (1992) the long-term trends derived from concurrent measurements of atmospheric CO_2 and O_2 have been widely used to quantify the partitioning of atmospheric CO_2 between the land-biosphere and oceanic sinks (Battle et al., 2000; Goto et al., 2017; Manning and Keeling, 2006; Valentino et al., 2008). This method hinges on the linear coupling between CO_2 and O_2 with an oxidation ratio (OR, defined as the stoichiometric ratio of exchange during various process such as photosynthesis and respiration expressed using α) of 1.1 for the terrestrial biosphere photosynthesis-respiration processes (α_b) and 1.4 for fossil fuel combustion (α_f) while they are decoupled for oceanic processes (α_o = 0). Meanwhile, the short-term variability in atmospheric oxygen can be used to estimate marine biological productivity and air-sea gas exchange (Keeling et al., 1998; Nevison et al., 2012). However, the accuracy of these estimates is primarily linked to the accuracy and precision of atmospheric O_2 measurements and the assumed ORs for the different processes which are highly variable in contrast to atmospheric CO_2 that can be well measured within the precision guidelines set by the Global Atmospheric Watch (GAW) ($\pm$ 0.1 ppm for the northern hemisphere).

Currently there are several, mostly custom built techniques that can measure atmospheric O_2 variations as oxygen concentration based on interferometric, paramagnetic, UV absorption and fuel cell technology (Keeling, 1988a; Manning et al., 1999; Stephens et al., 2007) or as O_2/N_2 ratios to account for the large background effect using gas

chromatography with thermal conductivity detector (GC-TCD) or gas chromatography coupled to mass spectrometry (GC-MS) (Bender et al., 1994; Tohjima, 2000). Despite the fact that these techniques have been used for more than two decades, accurate quantification of atmospheric oxygen variability remains challenging primarily because the small ppm-level atmospheric oxygen signal rides on a ~ 210,000 ppm background, which places stringent requirements on the precision and drift of the analysis methods especially for continuous monitoring(note that the GAW recommendation for the measurement precision of O_2/N_2 is 2 per meg). The techniques listed above struggle to routinely achieve the necessary performance for various reasons, including i) instability over time that requires frequent measurement interruption for calibration, ii) measurement bias with ambient and sample temperature and/or pressure, and/or iii) systematic errors in the measurement due to other atmospheric species. Further, some techniques require the use of consumables and rely on high vacuum, which complicates field deployment.

In this manuscript we describe a new high precision oxygen concentration and isotopic composition analyzer by Picarro Inc., Santa Clara, USA (G-2207) based on CRDS technology. Here, we will introduce the analyzer design principles in details, describe the unique features of the analyzer and evaluate its performance based on various independent laboratory and field tests by comparing it with currently existing techniques. Then, we will present and interpret our observations based on field measurements. Finally, we will conclude its overall performance and provide recommendations and possible improvements.

2. Analyzer design principles

The analyzer described here is derived from the Picarro G2000 series of CRDS analyzers. The basic elements have been described elsewhere (Crosson, 2008; Martin et al., 2016; Steig et al., 2014): briefly, the instrument is built around a high-finesse, traveling-wave

optical cavity, which is coupled to either of two single-frequency Distributed FeedBack-stabilized semiconductor lasers. One cavity mirror is mounted on a piezoelectric translator (PZT) to allow fine tuning of the cavity resonance frequencies. A semiconductor optical amplifier between the laser sources and the cavity boosts the laser power and serves as a fast-optical switch. The cavity body is constructed of invar and enclosed in a temperature stabilized box (T = 45° C, stabilized to approximately 0.01 °C) for dimensional and spectroscopic stability. A vacuum pump pulls the gas to be sampled through the cavity and a proportional valve between the cavity and the pump maintains the sample pressure in the cavity at a value of 340 hPa, with variations on the order of 1 Pa. The instrument has a wavelength monitor, based upon measurements of interference fringes from a solid etalon, which is used to control the laser wavelength by adjusting the laser temperature and current. The wavelength monitor is a fiber-coupled device located between the laser and the cavity. A fraction of the beam from the input fiber is collected using a beam splitter for the wavelength measurement and the remaining power is collected in the output fiber. A high-speed photodiode monitors the optical power emerging from the cavity. The instrument's data acquisition system is used to sweep the laser frequency over the spectral feature to be measured, modulates the laser output to initiate ring-downs, and fits the ring-down signal to an exponential function to generate a spectrogram of optical loss versus laser frequency. For this instrument the empty cavity ring-down time constant is about 39 μs. Subsequent program modules compare the measured loss spectrum to a spectral model, using non-linear least-squares fitting (Press et al., 1986) to find the best-fit model parameters and thereby obtain a quantitative measure of the absorption due to the target molecule, and finally apply a calibration factor to the optical absorption to deduce the molecular concentration. When operating in its normal gas analysis mode, the instrument acquires about 200-300 ring-downs

per second and achieves a noise equivalent absorption of typically about 10^{-11} cm^{-1} $Hz^{-1/2}$, with some variation between instruments.

The primary goal when designing this analyzer was to measure the molecular oxygen concentration with few-per-meg level precision and stability. In this context operational stability is as important as signal-to-noise. Our experience has been that the most stable operation of the analyzer is achieved when the optical phase length of the cavity is held as nearly constant as possible. In this case the free spectral range (FSR, 0.0206 cm^{-1}) of the temperature stabilized, invar ring-down cavity provides a better optical frequency standard than the etalon-based wavelength monitor, which in turn allows more consistent measurements of absorption line width and integrated absorption line intensity (Steig et al., 2014). For a small, field-deployable instrument, it is not practical to stabilize the absolute frequencies of the cavity modes to an optical frequency standard (Hodges et al., 2004) but the oxygen lines themselves, under conditions of constant temperature and pressure, provide an adequate frequency reference. The oxygen spectrum was also used to calibrate the FSR, by comparing a wide (approximately 10 cm^{-1}) FSR-spaced spectrum with the Hitran database (Rothman et al., 2013).

To determine molecular oxygen concentration, the analyzer measures absorption of the Q13Q13 component of the $a^1\Delta_g \leftarrow X^3\Sigma^-_g$ band, at 7878.805547 cm^{-1}, according to the latest edition of Hitran (Gordon et al., 2017). This is one of the strongest near-infrared lines of oxygen, well separated from other oxygen lines, and reasonably free of spectral interference from water, carbon dioxide, methane, and other constituents of clean air. The spectral model for this line was developed using reference spectra of clean, dry, synthetic air that were acquired with the same hardware as in the field-deployable analyzer, but with special-purpose software that allows it to operate as a more general spectrometer.

144 Recently, considerable work has been done to advance the understanding of spectral
145 line shapes and to define functional representations that better describe the processes that
146 determine spectral line shapes than does the Voigt model (Hartmann et al., 2008; Tennyson et
147 al., 2014, Tran et al., 2019). Line shape studies have been published for the 1.27 μm band of
148 O_2 (Fleisher et al., 2015; Lamouroux et al., 2014), though not to our knowledge for the Q
149 branch. The apparatus used here is not capable of spectroscopic studies of comparable
150 precision; the absolute temperature and pressure monitoring and especially the frequency
151 metrology are far too crude for that purpose. Our goal is merely to define a simple model of
152 the Q13Q13 line that is adequate for least-squares retrievals of the O_2 absorption under the
153 limited range of conditions (stabilized temperature and pressure) that the operational analyzer
154 experiences in the field. The CRDS analyzers use the Galatry function (Varghese and Hanson,
155 1984), which is distinctly better than the Voigt and still easily and quickly evaluated for line
156 shape modeling. Ultimately, the usefulness of the spectral model is to be evaluated by the
157 precision and stability of the O_2 measurements when compared with established techniques.
158 For spectral model development, this spectrometer has the drawback that the cavity FSR, is
159 too large to reveal much detail of the absorption line shape, even with the simplifying
160 assumption of a Galatry line shape. We therefore acquired a set of four interleaved spectra,
161 with the PZT-actuated mirror moved to offset the cavity modes of the individual FSR-spaced
162 spectra by one-fourth of an FSR. The precise offsets were determined from fits to the strong
163 and well-isolated O_2 lines in the spectra. From the consistency of the fitted line centers, we
164 estimate that the positioning of the interleaved spectra was accurate to approximately 10
165 MHz. The spectrum of the Q13Q13 line acquired in this manner is shown in Figure 1,
166 together with the best-fit Galatry function. It stands out that the residuals are largely odd in
167 detuning from the line center: this shows the limitations of the Galatry model in this case,

since the Galatry function is purely even about the line center. The shape of the absorption line in this model is specified by two dimensionless parameters: the collisional broadening parameter

$$y = \gamma / \sigma_D \quad (2)$$

and the collisional narrowing parameter

$$z = \beta / \sigma_D \quad (3)$$

where γ is the frequency of broadening transitions, β is the velocity change collision rate, and σ_D is the 1/e Doppler half-width of the transition, given by

$$\sigma_D = \nu_0 (2k_B T / Mc^2)^{1/2} \quad (4)$$

where ν_0 is the transition frequency, k_B is Boltzmann's constant (J. K^{-1}), T is the sample temperature (K), M is the molecular mass (amu), and c is the speed of light (m/s). Figure 2 shows the values of y and z obtained from spectra acquired in the same way as Figure 1, as a function of cavity pressure. The values depend linearly on pressure, as expected from the Galatry model, but the unconstrained linear fits do not go precisely through the origin. It is not clear whether this represents a breakdown of the Galatry model or simply reflects the limited quality of the data set. The slope of y can be converted to an air-broadened collisional width γ_{air} = 0.0442 cm^{-1}/atm, which agrees with the Hitran value of 0.0460 cm^{-1}/atm (Gordon et al., 2016) to within the uncertainty estimate stated by Hitran (uncertainty code 4 for γ_{air} corresponding to 10% --20% relative uncertainty). The slope of z can be interpreted in terms of the optical diffusion coefficient (Fleisher et al., 2015), yielding D = 0.285 cm^2 s^{-1}, compared to the literature value of 0.233 cm^2 s^{-1} for O_2 in air at 45 °C (Marrero and Mason, 1972). Although the anticipated use of the analyzer is for ambient air samples having a very small range of O_2 concentrations, we did investigate the variation of the line shape in binary mixtures of O_2 and N_2 shown in Figure 3. The error bars are taken from the output of the

Levenberg-Marquardt fitting routine (Press et al., 1992). The dependence of the collisional broadening parameter z on O_2 mole fraction was considered too small to be significant, but the variation in y was used in the subsequent analysis of the air samples. Note that Wójtewicz et al. (Wójtewicz et al., 2014) also found collisional broadening coefficients for nitrogen to be slightly larger than for oxygen in measurements of one O_2 line in the B-band.

The primary goal in designing the analyzer was to achieve high enough precision to make meaningful measurements of O_2 in clean atmospheric samples. Although the current best practice for such high-precision measurements is to work with dried samples, we decided to include high precision measurements of water vapor. There were two reasons for this decision: one is to serve as a monitor for residual water vapor, which is difficult to remove completely from the ring-down cavity and associated sample handling hardware, and the second and more ambitious reason was to see how well the effect of water vapor could be corrected for measurements of undried ambient air. While it was considered unlikely that measurements of undried air could compete in accuracy with those of dried air, it might be possible to correct for water vapor well enough to enable useful measurements in some circumstances without the expense and inconvenience of drying the sample. For this purpose, a second laser was added, which probes the $7_{1,6} \rightarrow 8_{4,5}$ component of the $2v_3$ band of water vapor, at of 7816.75210 cm^{-1} (Gordon et al., 2017). The Galatry model was used to fit spectra of synthetic air humidified to various levels of water vapor concentration. These fits also included two other nearby, very weak water lines, with intensities less than 1% of the strong transition, in order that their absorption should not perturb the line shape of the main transition. Results for the shape of the 7816.75210 cm^{-1} line are shown in Figure 4. At the level that we can measure, only the y-parameter has a meaningful variation with water concentration. From the linear fit one obtains a pressure broadening coefficient for air, γ_{air} =

0.0752 cm^{-1}/atm, in reasonable agreement with the Hitran value γ_{air} = 0.0787 cm^{-1}/atm (Gordon et al., 2017), and a self-broadening coefficient γ_{self} = 0.413 cm^{-1}/atm, to be compared with the Hitran value γ_{self} = 0.366 cm^{-1}/atm. Since the uncertainty estimate for the Hitran values is 10 % to 20 %, this level of agreement seems reasonable.

We also looked at absorption from water near the Q13Q13 absorption line of O_2. These spectra were measured in a background of pure nitrogen to reveal the very weak lines interfering with the O_2 measurement. Without the strong O_2 lines, it was impossible to interleave FSR-spaced spectra, so in this case the frequency axis comes from the analyzer's wavelength monitor. The upper panel of Figure 5 shows the spectrum of saturated water vapor in nitrogen, together with a fit to a Voigt model of the molecular lines. The measurement was made at a pressure of 340 hPa and temperature of 45° C. The main features are the Q13Q13 line from trace contamination of oxygen in the sample and several lines that arise from normal water ($^1H_2{}^{16}O$) and deuterated water ($^1H^2H^{16}O$ also abbreviated HDO). The lower panel of Figure 5 shows the lines tabulated in Hitran. Immediately after the data in Figure 5 were acquired, measurements were also made at 7816.85210 cm^{-1}, to establish the relationship between the absorption strengths in the two spectral regions. The relative intensities of the H_2O and HDO lines change with variations in the isotopic composition of the water, but fortunately the direct interference with the oxygen Q13Q13 lines comes entirely from the H_2O isotopologue, with the strongest HDO line being separated by approximately 8 line widths (FWHM) from the Q13Q13 line. Hitran simulations for molecules other than water that are expected to be present in clean, ambient air indicate that direct interference with the Q13Q13 line should be negligible at the level of precision considered here. In the case of CO_2, the dilution of oxygen due to 400 ppm of CO_2 is significant, and larger than any direct spectral interference.

239 Finally, we investigated the influence of water vapor on the shape of the O_2 Q13Q13
240 line. Switching between the two lasers sources, we acquired FSR-spaced spectra of
241 humidified synthetic air, alternately covering the 7817 cm^{-1} and 7878 cm^{-1} regions. Individual
242 spectra were acquired in less than 2 s, so changes in water vapor concentration between
243 spectra were small. These spectra, with frequency resolution of 0.0206 cm^{-1}, were analyzed by
244 nonlinear least-squares fitting with the following spectral models: the 7817 cm^{-1} spectra were
245 modeled as the sum of an empty-cavity baseline having an adjustable offset level and slope
246 and the water spectrum is modeled with three peaks: one strong line and two weak perturbers.
247 The molecular absorption of the main peak was expressed as an adjustable amplitude, A_w,
248 multiplying a dimensionless, area-normalized Galatry function (Varghese and Hanson, 1984).
249 The weak perturbers were modeled by Voigt profiles with amplitudes and line widths that
250 were constrained to be in fixed proportions to the strong line, and therefore added no new
251 degrees of freedom to the fitting procedure. Since the amplitude A_w multiplies an area-
252 normalized shape function, it is essentially equivalent to the area of the absorption line, to the
253 extent that the Galatry model provides a valid description of the line shape. The Doppler
254 width of the Galatry function was fixed based on the measured cell temperature, the y-
255 parameter was allowed to vary, and the z-parameter was constrained to be proportional to y,
256 based on measurements summarized in Figure 2. In addition, the center frequency of the
257 Galatry function was adjusted to match the data set, giving a total of five free parameters for
258 this fit. The 7878 cm^{-1} spectra were modeled with an adjustable baseline offset and slope and
259 molecular absorption amplitude, A_{O2}, describing the Q13Q13 O_2 line. Here, too, the y-
260 parameter and line center position of the O_2 lines were allowed to adjust, and the z-parameter
261 was constrained to be proportional to y. The weak water lines interfering with oxygen
262 absorption were included in the model, but with no additional free parameters; rather the

263 amplitudes were preset based on the measured water absorption at 7817 cm^{-1} and the
264 previously determined amplitude relationships between the water lines. This procedure does
265 not account for variations in HDO abundance, which may introduce some systematic error
266 into the water vapor correction for samples of unusual isotopic composition, but it should
267 accurately model the most important lines that interfere with the oxygen measurement.
268 Collisional broadening of the Q13Q13 O_2 line by water vapor is shown in Figure 6. From the
269 linear fit one obtains a coefficient for collisional broadening of the Q13Q13 line by water
270 vapor of γ_{water} = 0.0442 cm^{-1}/atm at 45 °C. Recently, parameters describing broadening of
271 oxygen lines by water vapor, obtained by empirical modeling of selected experimental
272 data, were added to the Hitran data base (Tan et al., In review). The new Hitran entries predict
273 a value of 0.0486 cm-1/atm at 45 °C, which is in agreement with our measurement within the
274 5-10% uncertainty attributed by Hitran to the broadening parameter. The alternating
275 measurements at 7817 cm^{-1} and 7878 cm^{-1} also calibrated the relationship between water mole
276 fraction and the absorption at 7817 cm^{-1}, using a dilution analysis described by Filges et al.
277 (2018), who showed that the results obtained this way agree well with water vapor fractions
278 measured with a conventional hygrometer. Figure 7 shows the measured amplitudes of the
279 water and oxygen lines for samples of variable humidity. Since the air came from a tank of
280 constant composition, the oxygen concentration changes due to dilution of oxygen when
281 water is added. Assuming that this is the sole cause of the change in measured absorption,
282 since the line shapes were being constantly adjusted to account for changes in collisional
283 broadening, it is straightforward to deduce the relation between the water fraction and the
284 absorption amplitude. This calibration was used to generate the water fraction axes in Figures
285 4 and 6. We note that we did not take particular care to control or measure the quantity of
286 dissolved gases, especially oxygen and carbon dioxide, in the water used for this experiment.

While these gases would not significantly affect the water calibration, they may affect the water vapor correction of the oxygen measurement at the ppm level. More work needs to be done to investigate the water vapor correction of the oxygen measurement.

The observations described above were used to design a method to measure oxygen concentration in ambient air. Gas from the inlet to the analyzer is drawn through the cavity at a rate of about 100 sccm (standard cubic centimeter per minute) and the conditions in the cavity are held stable at 340 hPa and 45°C. In its analysis mode the analyzer alternately measures ring-downs in the 7817 cm^{-1} and 7878 cm^{-1} regions. At 7878 cm^{-1} measurements are made at 11 different frequencies, spaced by one FSR of the cavity and centered at the peak of the Q13Q13 line. Multiple ring-down measurements are made to improve the precision of the loss determination, with a total of 305 ring-downs allocated to one spectrum. In the 7817 cm^{-1} region measurements are also made at 11 distinct frequencies at FSR spacings. Only 35 ring-downs are allocated to this spectral region, since the measurement of O_2 is much more important than water vapor. The data sets are analysed using a Levenberg-Marquardt fitting routine, which adjusts five free parameters in each region to find the best agreement to a spectral model based on Galatry line shapes, as described above. One of the outputs of the 7878 cm^{-1} fit is the frequency offset of the FSR grid from the center of the Q13Q13 line. This information is used to adjust the position of the PZT actuated mirror to keep the measurements centered on the line, effectively stabilizing the optical path length of the cavity to the frequency of the O_2 line. The reported water fraction is obtained by multiplying the fitted amplitude of the water line by a calibration constant derived from the dilution experiment as explained above. For the O_2 fraction a slightly more complicated procedure is followed. It was observed that the least-squares fitting of the data gives highly correlated results for the amplitude of the absorption line and the line width parameter y. The correlation

311 may be due in part to covariance of the fitted amplitude (proportional to line area) and line
312 width (Press et al., 1992) and it may also have a contribution from pressure variations that the
313 pressure sensor is unable to detect. The ratio A_{O2}/y can be determined from the fit much more
314 precisely than A_{O2} alone and so gives a more sensitive measurement of molecular absorption.
315 It also has the advantage of being independent of sample pressure, to the extent that the
316 Galatry model applies (Figure 2). However, using the ratio A_{O2}/y as a metric for absorption
317 adds more complications if measurements are to be made over a range of O_2 and water
318 concentrations, because the O_2/ N_2 ratio and the water concentration affect the line width
319 independently of pressure and O_2 concentration alone. To minimize systematic errors due to
320 these broadening effects, we define a nominal y-parameter based on the measured amplitudes
321 of the O_2 and water lines and the line broadening dependences shown in Figures 3 and 4. The
322 measured ratio A_{O2}/y is normalized by the nominal y to obtain a quantity that is ideally
323 independent of pressure and water concentration, and this is the quantity that is multiplied by
324 a calibration constant to give the reported O_2 fraction. In addition, a dry mole fraction is
325 reported for O_2, defined as the directly measured mole fraction corrected for water dilution.
326 The main goal in developing this instrument was to make high precision
327 measurements of O_2 mole fraction, based on absorption by the dominant $^{16}O_2$ isotopologue.
328 The absorption lines of the rarer isotopologues are also present nearby, so a mode of operation
329 was included in which one laser is scanned over neighboring lines of $^{16}O_2$ and $^{16}O^{18}O$ and the
330 ratio of amplitudes is used to derive an isotopic ratio, reported in the usual delta notation. In
331 this case the operating pressure was reduced to 160 hPa to improve the resolution of the
332 nearby lines. The lines measured were the Q3Q3 line of $^{16}O_2$, at 7882.18670 cm^{-1}, and the
333 Q9Q9 line of $^{16}O^{18}O$, at 7882.050155 cm^{-1}. The measurement procedure is very much like
334 that for the O_2 fraction measurement, so it will not be described in detail, only the main

differences will be noted. One is that in determining an isotopic ratio, normalizing absorption amplitudes by line widths does not provide any advantage, instead we simply take the ratio of amplitudes to compute delta. Although the Q9Q9 line and its neighbor Q8Q8 are the strongest ones in this band, absorption by $^{16}O^{18}O$ is still very weak, only about $5x10^{-9}$ cm^{-1} at the line center under the conditions we used. The signal-to-noise that can be achieved with this analyzer is not adequate to determine both the amplitude and the width of the $^{16}O^{18}O$ line with useful precision, so in the fitting step the y-parameter of the $^{16}O^{18}O$ line is constrained to be a constant factor times the fitted y-parameter for the $^{16}O_2$ line. Additionally, because of the weakness of the rare isotopologue absorption, the majority of ring-downs in each spectrum is devoted to measuring $^{16}O^{18}O$ i.e. 232 ring-downs in each spectrum versus only 40 for $^{16}O_2$. This implies that the mole fraction measurement in the isotopic mode is much less precise than when the analyzer measures the Q13Q13 line alone.

3. Results and Discussions

3.1. Laboratory tests at Picarro, Santa Clara

3.1.1. Temperature and pressure sensitivity

One set of tests was done to determine how well the goal was met of minimizing the susceptibility of the concentration measurements to noise or drift of the sample temperature and pressure. For these tests the analyzer sampled dry synthetic air from a tank and the temperature and pressure setpoints of the cavity were adjusted upward and downward from the nominal values, to obtain an estimate of the differential response. We express the sensitivity to experimental conditions in relative form, that is the derivative with respect to temperature or pressure divided by the signal under nominal conditions.

From these experiments, we determined a temperature sensitivity of $-2.1x10^{-4}$ K^{-1} and a pressure sensitivity of $+9.8x10^{-6}$ hPa^{-1}. The temperature sensitivity is somewhat larger than

359 expected based on a calculation using Hitran data to estimate the temperature dependences of
360 all the quantities that go into the measured absorption of the Q13Q13 line. The pressure
361 sensitivity is strikingly small, indicating a good cancelation of the pressure dependence of
362 absorption amplitude and line width. Both temperature and pressure sensitivities are small
363 enough to have a negligible effect on short-term precision of measurements made with the
364 stabilized ring-down cavity, though long-term drifts in the sensors are always a matter of
365 concern.

366 3.1.2. Measurement precision and drift

367 Measurement precision was evaluated by analyzing synthetic air containing nominal
368 atmospheric concentrations of CO_2 and CH_4 from an aluminum Luxfer cylinder over a period
369 of several days. The tank, oriented horizontally and thermally insulated (though not
370 controlled), was connected directly to the instrument (S/N TADS2001) with a 2-stage
371 pressure regulator and stainless-steel tubing with an additional orifice to about 55 sccm. For
372 the isotopic mode of operation, the precision of the measurement was also tested by making
373 repeated measurements from a tank of clean, dry synthetic air.

374 Figure 8 shows the time series of the precision test data, displaying the reported
375 oxygen concentration, the height of the oxygen absorption peak, the width of the oxygen
376 absorption peak and the ambient temperature. The residual error of the analyzer, although
377 small, is nevertheless significant given the stringent targets set forth by the WMO-GAW
378 program. Possible sources of error include: temperature drifts due to sensor drift or gradients;
379 pressure errors due to sensor drift; optical artifacts such as parasitic reflections, higher order
380 cavity mode excitation, and/or loss nonlinearity that can distort the reported oxygen spectrum.
381 More work is required to identify and eliminate these small drifts.

382 The Allan standard deviation of the reported O_2 fraction is shown in the Allan-Werle
383 plot in Figure 9. The ordinate on this plot is the square root of the Allan variance of reported
384 mole fraction, so 1 ppm in these units corresponds to about 5 per meg in the ratio of O_2/ N_2.
385 The precision of averaged measurements improves as $\tau^{-1/2}$ for approximately 5000 s and
386 reaches 1 ppm in less than 10 minutes and remains below 1 ppm for time scales on the order
387 of about 1 hour (τ is the averaging time which is the abscissa of the Allan-Werle plot).

388 Figure 10 shows the precision of $\delta(^{18}O)$ (uncalibrated) derived from the ratio of lines
389 measured at 7882 cm^{-1}. Because of the weak signal from the $^{16}O^{18}O$ line, it is necessary to
390 average for more than 20 seconds or more to achieve 1‰ precision on the isotopic ratio. As
391 for the concentration measurement, averaging improves the measurement precision for time
392 scales up to about 1 hour.

393 **3.2. Laboratory measurements at the University of Bern**

394 3.2.1. Measurements of standard gases

395 The performance of the instrument was tested by analyzing eight standard gases with
396 precisely known CO_2 and O_2 compositions (Table 1) using the CRDS analyzer and comparing
397 it to parallel measurements with a paramagnetic oxygen sensor (PM1155 oxygen transducer,
398 Servomex Ltd, UK) embedded to a commercially available fuel cell oxygen analyzer
399 (OXZILLA II, Sable Systems International, USA) (Sturm et al., 2006) as well as with an
400 isotope ratio mass spectrometer (IRMS, Finnigan Delta^{Plus}XP). The design of the
401 measurement set-up is shown in Figure 11. Standard gases were directly connected to the
402 pressure controlling unit, and a multi-port valve (V2) was used to select among the standard
403 gases. Flow from each cylinder was adjusted to about 120 sccm which was eventually
404 directed to a selection valve (V1), allowing switching between ambient air and standard gases.
405 Flow towards and out of the fuel cell analyzer was controlled by the pressure controlling unit.

406 The O_2 mixing ratio of this incoming gas was first measured on the Paramagnetic O_2 sensor
407 and then directed towards a non-dispersive infrared analyzer (NDIR) (Li-7000, LICOR, USA)
408 for measuring CO_2 and H_2O. The outflow from this analyzer (100 sccm) returns to the
409 pressure controlling unit and was eventually divided between the CRDS analyzer (which uses
410 about 75-80 sccm) and the IRMS (~ 20 sccm) via a Tee-junction. Each cylinder was measured
411 for two hours in each system controlled by a LabView program.

412 First, we investigated the influence of this Tee-junction, which splits the gas flow
413 between the CRDS and the IRMS, on the measured O_2 values. Manning (2001) showed that
414 the fractionation of O_2 in the presence of a Tee-Junction is strongly dependent on the splitting
415 ratios as well as temperature and pressure gradients. Hence, we measured and compared the
416 O_2 mixing ratios of two standard gases (CA07045 and CA060943) in two cases: i) in the
417 presence of a Tee-junction with different CRDS to IRMS splitting ratios and ii) without a
418 Tee-junction so that all gas flow is directed towards the CRDS analyzer. The splitting ratios in
419 these test experiments vary from 1:1 to 1:100, and reversed to change the major flow direction
420 either to the CRDS or the IRMS. Note that the experimental condition in this manuscript is
421 with a 4:1 splitting ratio (i.e. ~ 80 sccm towards the CRDS analyzer and ~ 20 sccm towards
422 the IRMS).

423 In the cases of the smaller splitting ratios (1:1, 1:4 and 4:1), which are relevant for the
424 results presented in this study, only minor differences in the measured O_2 mixing ratios were
425 observed when compared to case ii (i.e. without a Tee-junction). For these two cylinders
426 measured, the average differences in these cases were about 0.5 ppm, calculated as the mean
427 of the differences in the raw O_2 measurements of the last 60 seconds. The negligible
428 fractionation can indeed be the result of smaller splitting ratios while strong influence is
429 usually expected in case of larger splitting ratios (Stephens et al., 2007). For higher splitting

ratios, the result seems inconclusive without any dependence on the ratios due to the strong decline in the cylinder temperature (specifically at the pressure gauge) caused by higher flow to achieve the higher splitting ratios (as high as 1:100). Hence, these tests need to be conducted in a temperature-controlled condition and the results could not be discussed in this manuscript.

Figure 12 shows the standard gas measurements for the seven cylinders with known CO_2 and O_2 mixing ratios (Table 1) using both the CRDS and the Paramagnetic analyzers. Standard eight, which has too high O_2, is not shown in the figure as the figure is zoomed-in to better illustrate the change in O_2 for the remaining cylinders. While the first five cylinders contain O_2 and CO_2 mole fractions comparable to ambient air values, standards 6 & 8 had either very low or very high O_2, respectively. In addition, standards 6 and 7 have very low and very high CO_2 mixing ratios. Note that due to its very high CO_2 content (~ 2700 ppm), standard 7 was not measured on the IRMS and hence the O_2 mixing ratio is unknown. The measured mixing ratios for the six standard gases measured with the two systems are in very good agreement while cylinder 7 showed an opposing signal for the two analyzers compared to standard 6 (Figure 12). While the Paramagnetic analyzer showed a higher O_2 mixing ratio, the values from the CRDS analyzer are lower in O_2. This can be associated with the very high CO_2 mixing ratio in standard 7, which leads to a strong dilution effect in the CRDS analyzer as it does not include any correction function for dilution effect from CO_2. However, such high CO_2 mixing ratios may not be that important for most atmospheric research. Yet, it should be considered to include a parallel CO_2 mixing ratios measurement to the instrument as it will further improve the accuracy. This would be especially important for biological or physiological studies where a wide range of CO_2 and O_2 concentrations must be expected.

453 The measurement precision of the CRDS analyzer was calculated as the standard error
454 of the mean i.e. the standard deviation (1-σ) of the last 1-minute raw measurements divided
455 by the square root of the number of measurements (n = 60), and for all these cylinders the
456 values are usually between 0.5 ppm to 0.7 ppm. For parallel measurements of these cylinders
457 using a Paramagnetic analyzer, we obtained a precision of about 1 ppm, calculated exactly the
458 same way.

459 We also made a correlation plot to see which of the two instruments are in better
460 agreement with the assigned values based on IRMS measurements for the individual
461 cylinders. While similar correlation coefficients were observed for both analyzers, different
462 slopes were calculated (Fig. A.1). This is due to the fact that the IRMS measures the O_2 to N_2
463 ratio ($\delta(O_2/N_2)$) in per meg, while the CRDS and the Paramagnetic analyzers provide non-
464 calibrated O_2 mixing ratios in units of ppm and per meg, respectively. If we exclude the two
465 standard gases with the highest and lowest O_2 mixing ratios (standards 7 and 8) that are
466 subjected to strong dilution effects, both the slope and the r^2 values decrease from those
467 shown in Figure A.1. But this decrease is larger in the case of the Paramagnetic
468 measurements, implying a slightly better linearity of the CRDS analyzer.

469 3.2.2. Measurements of ambient air

470 Ambient air measurements were conducted from the roof top of our laboratory at the
471 University of Bern to evaluate the analyzer's performance under atmospheric variability.
472 Ambient air was continuously aspirated from the inlet at the roof of the building at a flow rate
473 of ~ 250 sccm which is then dried using a cooling trap kept at -90 °C towards the switching
474 valve (V1) and measured in similar way to the standard gases as explained above. The
475 measurement values obtained here were compared with the parallel measurements by the
476 Paramagnetic sensor to test the instruments stability and accuracy.

Figures 13 panels a &b show the 1-minute average ambient air measurements from the rooftop inlet by the Paramagnetic and the CRDS analyzers at the beginning of the testing period including standard gases measured every 12-hour. While the Paramagnetic analyzer seems to be stable, the CRDS analyzer showed a strong drift for an extended period. This can be due to unstable conditions in the CRDS measurement system as it started operating right after it was unpacked. Hence, we looked into temperature inside the instrument chassis and pressure records, which were stable within the manufacturer's recommended range during this period. As the CRDS analyzer incorporates a water correction function, interference from this species should be well accounted. Even comparing the analyzer's parallel water measurements to water measurements by the NDIR system such a drift was not observed. It should be noted that the two internal standard gases which were less frequently measured (every 12 hours) during this period were also drifting following similar pattern. This implies that the drift is associated with the analyzer. Interestingly, this pattern can be modeled using a polynomial function which can then be used to correct for the observed drift in the ambient air measurements. After applying a polynomial drift correction, we were able to fully accounted for the observed drift. However, the manufacturer decided to further investigate possible causes of this drift. After further improvements, we obtained the first commercial analyzer in September 2017 and repeated the above tests (Figure 13 c &d). No such drift was observed any more in the standard gases or in ambient air measurements.

We believe that the optical amplifier has caused the drift in the first system and not anymore included in the design of the product which produced a significant amount of broadband light that could fill the cavity (albeit with a low coupling coefficient), and would ring down with a different (and generally much faster) time constant that the baseline loss of the cavity. However, the ringdown time on the peak of the oxygen line is just 10 microseconds, such that

501 the broadband light might have distorted the single exponential decay of the central laser
502 frequency, leading to the observed drift in the oxygen signal. However, we were not able to
503 confirm this hypothesis.

504 3.2.3. Water correction test

505 Measurements of oxygen are reported as both wet ($O_{2,\ raw}$) and dry ($O_{2,\ dry}$) mole
506 fractions by the CRDS analyzer as it also measures water vapor in parallel at its water
507 absorption line (7817 cm^{-1}), and corrects for the dilution effect based on an inbuilt numerical
508 function:

509 $$O_{2,dry} = \frac{O_{2,raw}}{1 - f_{H_2O}} \qquad (5)$$

510 where f_{H2O} is the measured water mole fraction.

511 The efficiency of water correction by this function was assessed in two ways: i) by comparing
512 the water vapor content in standard air measured by this analyzer with similar measurements
513 by the NDIR analyzer and ii) by comparing the oxygen mixing ratios between non-dried
514 ambient air measured and corrected for water dilution by the CRDS analyzer with dried air
515 measured using a paramagnetic analyzer.

516 Figure 14 shows the water vapor content for standard gases measured continuously for
517 two days by the CRDS and the NDIR analyzers. Note that the two data sets are manually
518 fitted to each other as the measured water values by the NDIR analyzer are not calibrated.
519 Based on this plot, the two analyzers are in very good agreement although there are small
520 differences during very dry conditions (low water content).

521 Figure 15a shows the dried ambient air water measurements in both analyzers with
522 frequent spikes due to valve switching while measuring standard gases. In the second case,
523 where the water trap was by-passed and non-dried air was allowed to the CRDS analyzer

keeping the dried air flow to the NDIR (Figure 15b), a clear increase in the water measurements in the CRDS analyzer can be observed. Here, it should be noted that there are no spikes in the water measurements of the CRDS analyzers as there are no standard gas measurements in between and the inlet is directly connected to the CRDS analyzer (Figure 11). Figures 15c & 15d show the difference in oxygen measurements of ambient air measured in both analyzers in the two cases stated above (note that the CRDS uses its built-in water correction function applying Eq. 5). The measurements of the Paramagnetic analyzer were scaled to ppm units by applying the correlation equation obtained from the six standard gas measurements of the two analyzers (Fig. A.1). Note that the CRDS measurements were corrected for the observed drift using the polynomial fit to the two standard gas measurements stated above.

In the first period of the measurement when both analyzers measured dried ambient air, the absolute differences between the 1-minute averages measured over two days by the two analyzers were mostly within 15 ppm (Figure 15c) and symmetrically distributed around zero (Figure 15e). However, when wet air was admitted to the CRDS analyzer and the in-built water correction was applied, a stronger variability was observed in the calculated differences (Figure 15d). This implies stronger short term variability in the CRDS analyzer measurement values (as nothing was changed for the Paramagnetic measurement system) when wet samples were analyzed. The more negative values in the differences (Figure 15f) can also be associated with overestimation of the O_2 mixing ratios by the CRDS originating from an overestimated water correction. However, detailed evaluation of the analyzer's water correction function is beyond the scope of this study.

3.3. Field Measurements

After a series of tests at University of Bern, we conducted multiple field measurements at the High Altitude Research Station Jungfraujoch and the Beromünster tall tower sites in Switzerland described below.

3.3.1. Tests at the High Altitude Research station Jungfraujoch

The High Alpine research station Jungfraujoch is located on the northern ridge of the Swiss Alps (46° 33′ N, 7° 59′ E) at an elevation of 3580 m a.s.l. It is one of the global atmospheric watch (GAW) stations well-equipped for measurements of numerous species and aerosols. The site is above the planetary boundary layer most of the time due to its high elevation (Henne et al., 2010; Zellweger et al., 2003). However, thermally uplifted air from the surrounding valleys during hot summer days or polluted air from the heavily industrialized northern Italy may reach at this site (Zellweger et al., 2003). The Division of Climate and Environmental Physics at the University of Bern has been monitoring CO_2 and O_2 mixing ratios at this site based on weekly flask sampling and continuous measurements since 2000 and 2004, respectively (Schibig et al., 2015). The CO_2 mixing ratio is measured using a commercial NDIR analyzer (S710 UNOR, SICK MAIHAK) while O_2 is measured using the Paramagnetic sensor (PM1155 oxygen transducer, Servomex Ltd, UK) and fuel cells (Max-250, Maxtec, USA) installed inside a home-built controlling unit. Similar to the comparison tests at the University of Bern, we have conducted parallel measurements between the CRDS analyzer and the paramagnetic cell at this high altitude site during 03 – 14 February 2017. The measurement of ambient air at the Jungfraujoch system is composed of sequential switching between low span (LS) and high span (HS) calibration gases followed by a target gas (T) measurement (once a day) to evaluate the overall system performance and finally a working gas (WG) measurement before switching back to ambient air.

570 Figure 16 (top panel) shows the calibrated 1-minute averaged O_2 mixing ratios
571 measured at this high altitude site in comparison with the Paramagnetic oxygen analyzer
572 already available at the site. Despite the strong variability observed during the measurement
573 period of 10-days by both analyzers, a very good agreement was observed between them.
574 Figure 16 (bottom panel) shows the absolute difference of 1-minute averages in
575 atmospheric O_2 measured at Jungfraujoch between the two analyzers which are mostly within
576 ±5 ppm range (but sometimes going as high as ±10 ppm) without an offset. However, for
577 generally reported 10-minutes, half-hourly or hourly means these values correspond to < 1.5
578 ppm, < 1 ppm and < 0.65 ppm.
579 3.3.2. Tests at the Beromünster tall tower site
580 The Beromünster tower is located near the southern border of the Swiss Plateau, the
581 comparatively flat part of Switzerland between the Alps in the south and the Jura mountains
582 in the northwest (47° 11′ 23″ N, 8° 10’ 32″ E, 797 m a.s.l.), which is characterized by intense
583 agriculture and rather high population density. A detailed description of the tower
584 measurement system as well as a characterization of the site with respect to local
585 meteorological conditions, seasonal and diurnal variations of greenhouse gases, and regional
586 representativeness can be obtained from previous publications (Berhanu et al., 2016; Berhanu
587 et al., 2017; Oney et al., 2015; Satar et al., 2016). The tower is 217.5 m tall with access to five
588 sampling heights (12.5 m, 44.6 m, 71.5 m, 131.6 m, 212.5 m) for measuring CO, CO_2, CH_4
589 and H_2O using Cavity Ring Down Spectroscopy (Picarro Inc., G-2401). By sequentially
590 switching from the highest to the lowest level, mixing ratios of these trace gases were
591 recorded continuously for three minutes per height, but only the last 60 seconds were retained
592 for data analysis. The calibration procedure for ambient air includes measurements of
593 reference gases with high and low mixing ratios traceable to international standards (WMO-

X2007 for CO_2 and WMO-X2004 for CO and CH_4), as well as target gas and more frequent working gas determinations to ensure the quality of the measurement system. From two years of data a long-term reproducibility of 2.79 ppb, 0.05 ppm, and 0.29 ppb for CO, CO_2 and CH_4, respectively was determined for this system (Berhanu et al., 2016).

Between 15.02.2017 and 02.03.2017, we have connected the new CRDS oxygen analyzer in series with the CO_2 analyzer (Picarro G-2401) and measured the O_2 mixing ratios at the corresponding heights. Similar to the CO_2 measurements, O_2 was also measured for three minutes at each height. During this period, we have evaluated the two features (isotopic mode and concentration mode) of the CRDS analyzer. In the isotopic mode, the CRDS measures the $\delta^{18}O$ values as well as the O_2 concentration while in concentration mode only the latter was measured.

During the tests conducted at this tower site, we first evaluated the two operational modes (concentration vs isotopic modes) of the CRDS analyzer. Ambient air measurements on isotopic mode over a 4-days period showed a strong variability in the measured oxygen mixing ratios and it was not possible to distinguish the variability in the O_2 mixing ratios among the five height levels. The calculated 1-minute standard error for ambient air measurements was as high as 10 ppm while a standard error of less than 1 ppm was determined from similar measurements in the concentration mode. Additionally, comparing the O_2 values between the two modes, frequent short time variation in ambient air O_2 (~ 200 ppm) was observed in the isotope mode measurements while the variation in the concentration mode is significantly smaller (~ 30 ppm). This precision degradation is due to the weaker ^{16}O oxygen line used for the isotopic mode, and the fact that far more ring-downs are collected on the rare isotopologue in isotopic mode Hence, we have conducted the remaining test measurements in concentration mode.

618 As this tower has five sampling height levels, we first followed three minutes of
619 switching per inlet level, which enables four measurements per hour at a given level.
620 However, we noticed hardly any difference among the different levels due to strong short
621 term variability in O_2 mixing ratios between the consecutive heights. Hence, we switched to a
622 longer sampling period of six-minutes per height. Figure 17 shows the diurnal CO_2 and O_2
623 variations at the lowest (12 m) and highest (212.5 m) sampling heights of the tower. These
624 two heights were selected simply to better illustrate the difference in the mixing ratios. The
625 CO_2 mixing ratios on the top panel show higher values at the 12 m inlet than the highest level
626 most of the day due to its closeness to sources except during the afternoon (11:00 - 17:00
627 UTC) when both levels show similar but decreasing CO_2 mixing ratios. This is due to
628 presence of a well-mixed planetary boundary layer (PBL) (Satar et al., 2016). The lag in CO_2
629 peak between the two height levels by about two hours indicates the duration for uniform
630 vertical mixing along the tower during winter 2017. The opposite variability patterns are also
631 clearly visible in the O_2 mixing ratios shown in the lower panel with a clear distinction
632 between the two height levels during early in the morning and in the evening while similar O_2
633 values were observed in the afternoon. These opposing profiles are expected as CO_2 and O_2
634 are linearly coupled with a mean oxidation ratio of -1.1 ± 0.05 (Severinghaus, 1995) for land-
635 biospheric processes (photosynthesis and respiration) and -1.44 ± 0.03 for fossil fuel burning
636 (Keeling, 1988b).

637 Table 2 shows the oxidation ratios derived as the slopes of the linear regression
638 between CO_2 and O_2 mixing ratios at the different height levels measured on 25 February
639 2017. Accordingly, height dependent slopes were observed with a slope of -0.98 ± 0.06 at the
640 lowest level, close to the biological processes induced slope but slightly lower than its mean
641 value. For the highest level, we calculated a slope of -1.60 ± 0.07 a value close to fossil fuel

combustion oxidation ratio. Note that depending on fossil fuel type the oxidation ratio can range between -1.17 and -1.95 for coal and natural gas, respectively (Keeling, 1988b). While the slopes derived for the two other levels (44.6 m and 131.6 m) show similar values between the highest and lowest height levels, possibly from mixed sources, the middle level showed a slightly higher slope than these two levels but still in the large range between the lowest and highest inlet heights.

3.4. Evaluation of the $\delta^{18}O$ measurements

To further evaluate the analyzer's performance in measuring stable oxygen isotopes, we conducted ambient air isotopic composition measurements as well as analyzed a standard gas without CO_2 which has a known $\delta^{18}O$ value. The choice of this CO_2-free air standard gas is twofold: one it has a known $\delta^{18}O$ value and second as it has no interference from possible CO_2 absorption band overlap. For this test three 0.5 L glass flasks were preconditioned and filled with this standard gas to ambient pressure. These flasks were attached before or after the water trap (Fig. 11) and measured similar to ambient air measurements. These measurements were then compared with $\delta(^{34}O/^{32}O)$ values obtained by parallel measurements using our IRMS.

Figure 18 shows the $\delta^{18}O$ values of ambient air from the roof top with three consecutive measurements of glass flasks filled with CO_2-free air in-between followed by a fourth flask filled with breath air. An excellent agreement was observed for measurements from both instruments for the three flasks filled with a standard gas. However, the fourth flask with breath air showed a signal opposite to the measurements by the IRMS. As breath air contains large amount of water and CO_2 in addition to O_2, which can possibly interfere with the CRDS analyzer measurements, we have removed H_2O and CO_2 by using a cryogenic trap (-130 °C) and in an additional experiment using Schütze reagent to remove both CO and CO_2.

However, we have not observed any improvement towards an agreement with the IRMS measurements. Therefore, any other gas component in the breath air must be relevant for the interference. Based on the absorption lines in the spectral range of the instrument (7878 cm^{-1}) retrieved from HITRAN database, we expect interference either from carbon monoxide (now excluded by the tests) or methane or VOCs including acetone, ethanol, methanol or isoprenes, all of which have been measured in breath air (Gao et al., 2017; Gottlieb et al., 2017; Mckay et al., 1985; Ryter and Choi, 2013; Wolf et al., 2017). Further investigations have to shed light on these interferences in order to take corresponding action to surpass these shortcomings in the isotope analysis based on cavity ring-down spectroscopy.

4. Conclusions

We have thoroughly evaluated the performance of a new CRDS analyzer which measures O_2 mixing ratios and isotopic composition combining laboratory and field tests. Even if a drift in the analyzer was observed at the beginning of this study, which can be easily corrected by calibration, the recent analyzers built by the manufacturer did not show such instrumental drift. However, prior tests are recommended to see the analyzer's stability.

The T-split tests for the current measurement setup based on the measurements of two standard gases showed a difference within the measurement uncertainty. However, this effect may become significant while applying larger splitting ratios and we recommend conducting further experiments to accurately quantify this influence for larger splitting ratios.

We have observed a strong influence of dilution in the measured O_2 values during the presence of high CO_2 mixing ratios. Even if such an influence may not be critical for the present study, such an effect might be significant in other studies where higher CO_2 mixing ratios might be present and we recommend following a correction strategy based on parallel CO_2 measurements. This also applies for more accurate analysis.

690 The water correction applied by the instrument's in-built function seems to sufficiently
691 correct for the water vapor influence. However, a larger variability of the difference was
692 observed between the CRDS analyzer and the Paramagnetic cell when dried samples were
693 used in both systems. This can possibly be due to an overcorrection by the water correction
694 function of the CRDS analyzer when dried samples were used. This is particularly true for the
695 very low water vapor range (< 100 ppm). We believe that it is important to further investigate
696 this issue and identify an improved water correction strategy.

697 Based on the analysis of O_2 mixing ratios in the concentration and isotopic modes, we
698 have observed a significant decrease in precision (about ten-fold) in the latter measurement
699 mode. The measured $\delta^{18}O$ values for the standard air by the CRDS analyzer are in excellent
700 agreement with the IRMS values. However, such measurements for a breath air showed a
701 contrasting signal, possibly due to interference from other gases such as CH_4. Hence, we
702 recommend further investigation on such possible contaminants and how to possibly remove
703 them while conducting ambient air measurements. However, we believe that this analyzer can
704 be used for tracer experiments where artificially enriched isotopes are used to study biological
705 processes such as photosynthesis in plants using isotopically labelled CO_2 and H_2O.

706 **Acknowledgement**

707 We would like to thank ICOS-RI and the Swiss National Science Foundation (SNF) for
708 funding ICOS-CH (20FI21_148994, 20FI21_148992). We are also grateful to the
709 International Foundation High Alpine Research Stations Jungfraujoch and Gornergrat. The
710 measurement system at the Beromünster tower was built and maintained by the CarboCount-
711 CH (CRSII2_136273) and IsoCEP (200020_172550) projects both funded by SNF.

712

713

List of Tables

Table 1. Assigned mixing ratios of standard gases used in this study and their corresponding values measured by the NDIR, CRDS and IRMS at the University of Bern. [1]The assigned values are based on measurements from different institutions (University of Bern (UB), Scripps or NOAA, see column cylinder name). [2]Measurements are on the Bern scale for CO_2 and O_2. The Bern scale is shifted by +550 per meg. [3]Values on the Scripps scale.

Cylinder name	Assigned CO_2 (ppm) [1]	Assigned O_2 (per meg) [1]	CO_2-IRMS (ppm) [2]	CO_2-NDIR (ppm) [2]	O_2-IRMS (per meg) [2]	O_2-Paramagnetic (per meg) [2]	O_2-CRDS (per meg)[2]
ST-1 LUX3576-UB	427.47	-1026	427.47	427.59	-1026	-1070	-1057
ST-2 LK922131-UB	368.09	599	368.09	367.82	599	560	590
ST-3 CA07045-Scripps	382.303	-271.6	382.50	381.99	278 (-272.2)[3]	302	281

ST-4 CA07043-Scripps	390.528	-476.4	390.69	390.15	71 (-479.5)[3]	66	63
ST-5 CA07047-Scripps	374.480	-807.7	374.70	374.17	-253 (-803.3)[3]	-212	-233
ST-6 CA04556-NOAA	192.44	-3410	191.21	191.64	-3410	-2905	-3013
ST-7 CA06943-NOAA	2699.45	-		2612.80	-	-2691	-3369
ST-8 LK76852-UB	411.49	37794	411.49	406.25	37794	34513	36017

728

729

730 Table 2. The CO_2 and O_2 correlation coefficients at the different height levels derived using
731 the least square fit and the correlation coefficients (r^2). Uncertainties are calculated as
732 standard error of the slope.

Height	Oxidation Ratios (O_2:CO_2)
12.5 m	-0.98 ± 0.06 (0.48)
44.6 m	-1.29 ± 0.07 (0.50)
71.5 m	-1.49 ± 0.08 (0.47)
131.6 m	-1.23 ± 0.05 (0.55)
212.5 m	-1.60 ± 0.07 (0.61)

733

734

735

736

737

738

739

740

741 List of Figures

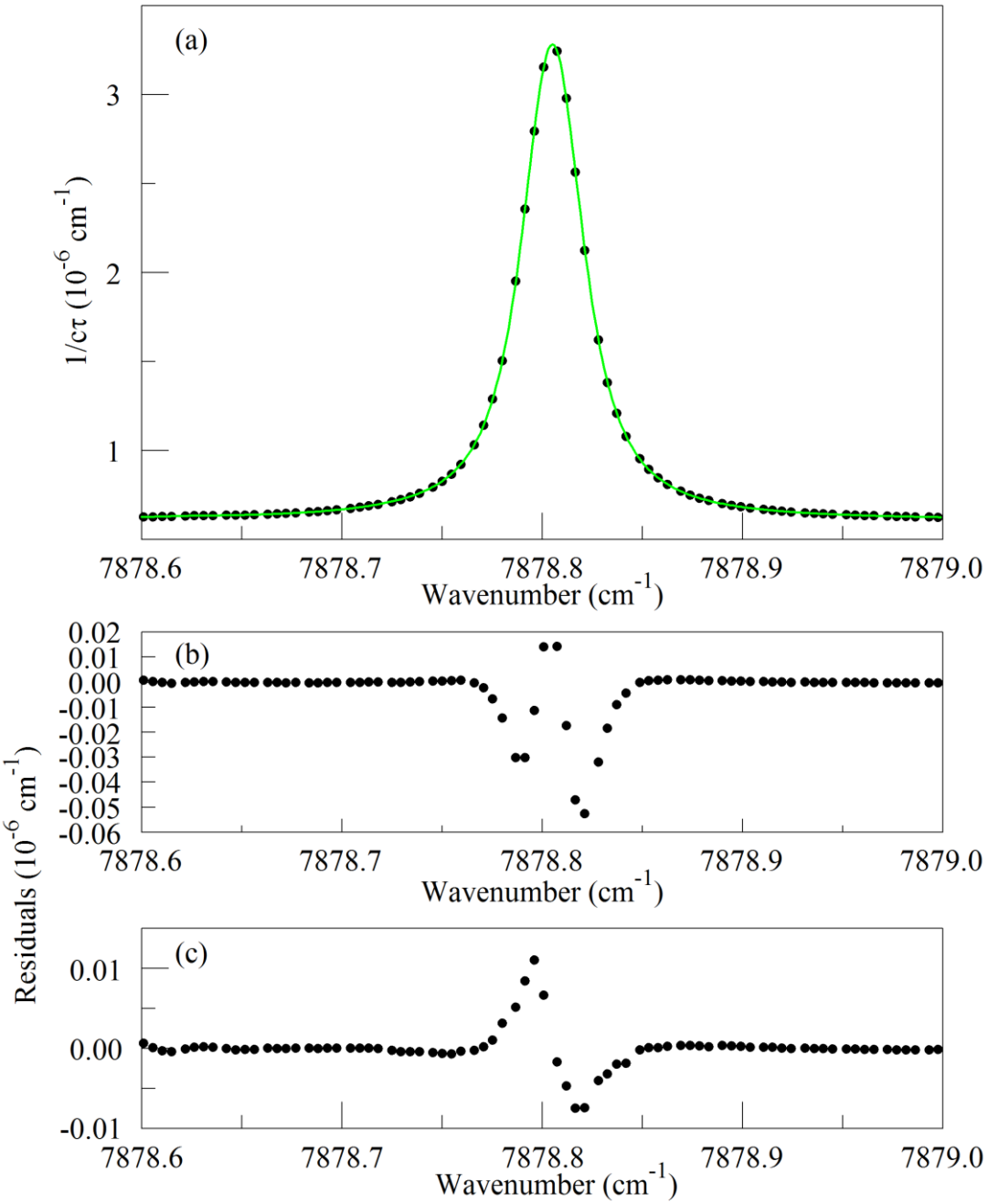

742

743 Figure 1. The top panel (a) shows the raw data (points) and the best-fit Galatry function (solid
744 line). Residuals of the Voigt fit are shown in panel (b) and residuals of the Galatry fit are
745 shown in panel (c).

746

747

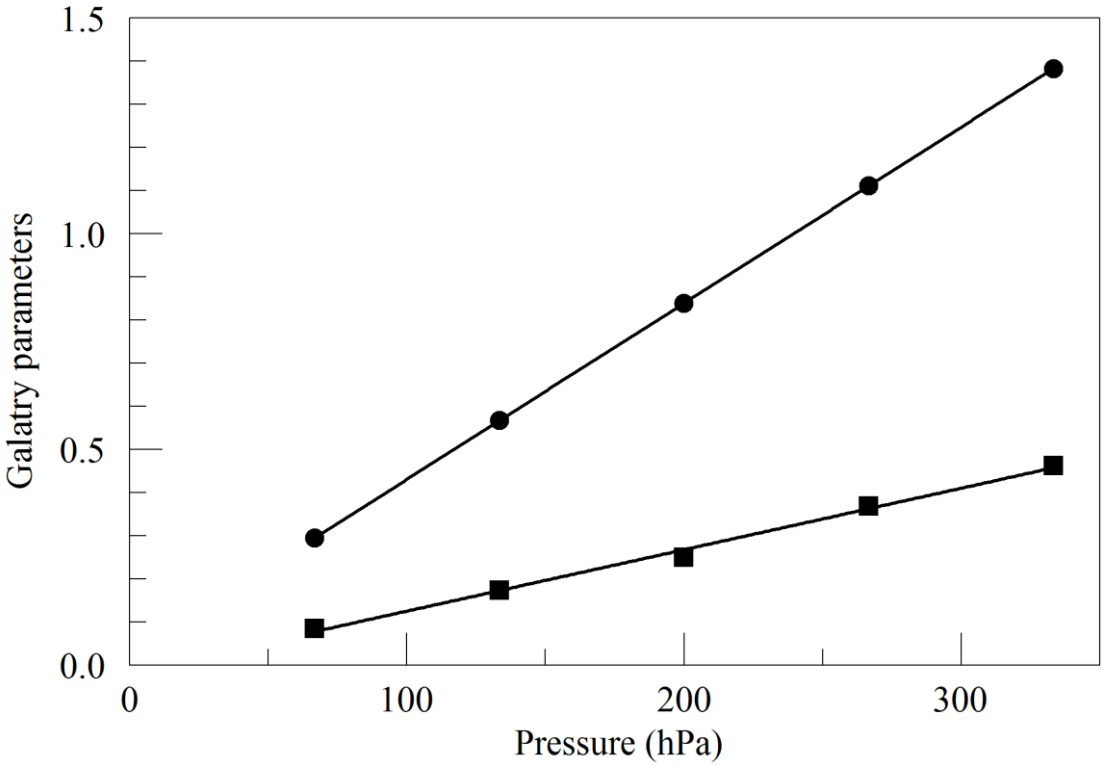

748

749 Figure 2. Best-fit values for the Galatry parameters of the Q13Q13 line of O_2, as a function of
750 pressure. The line broadening parameter y is represented by circles and the line narrowing
751 parameter z by squares. The solid lines are linear fits to the measurements. The best-fit offset
752 and slope are 0.0227 and 0.004082 hPa^{-1} for y, and -0.0169 and 0.001424 hPa^{-1} for z.

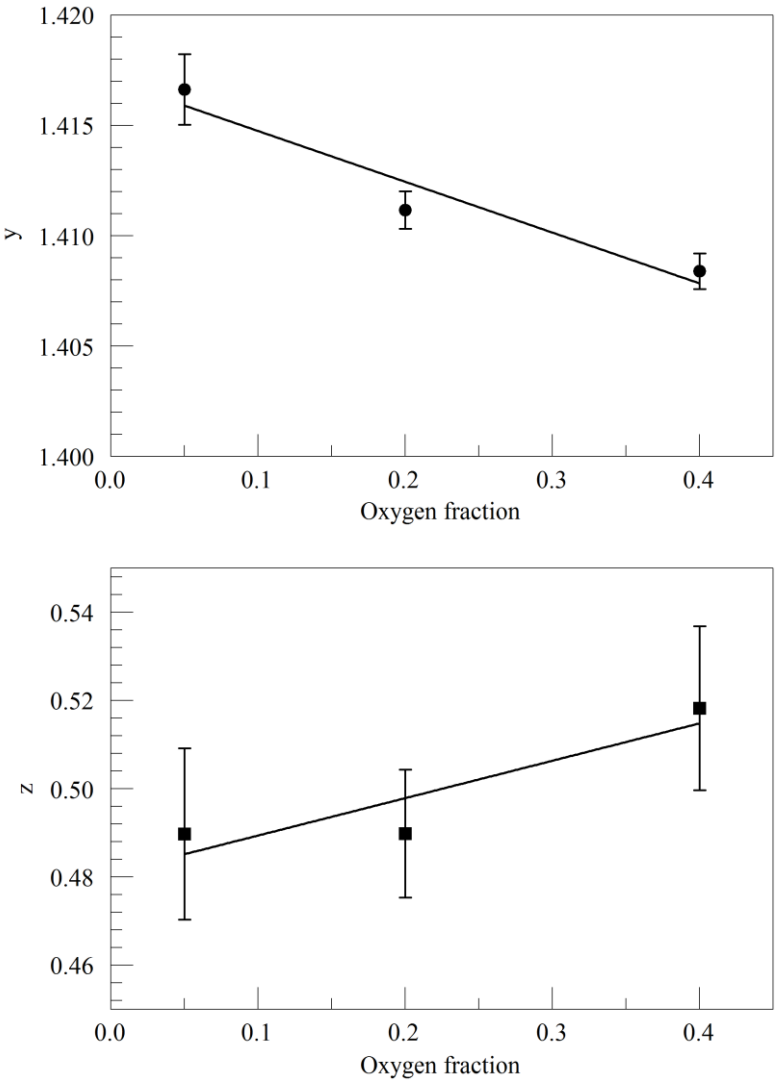

753

754 Figure 3. Galatry parameters of the Q13Q13 line of O_2 at 340 hPa and 45° C as a function of

755 O_2 mole fraction in binary O_2 - N_2 mixtures. The linear fits to the data are y = 1.417 – 0.023 x

756 f_{O2} and z = 0.481 + 0.085 x f_{O2}.

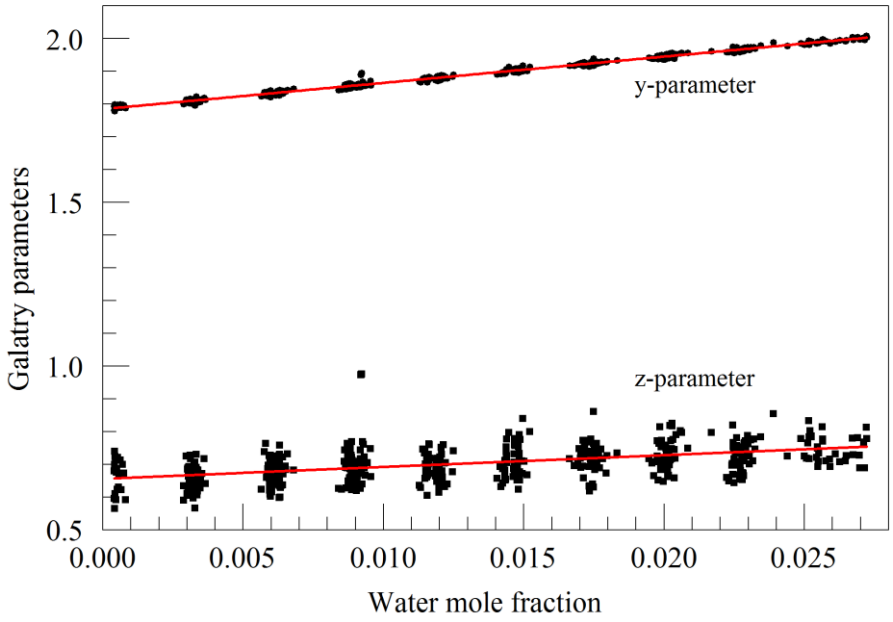

Figure 4. Galatry parameters of the 7816.75210 cm^{-1} water line in air at 340 hPa and 45° C as a function of water mole fraction. Black points are from measurements and red lines are linear fits: $y = 1.7846 + 8.01 \times f_{H2O}$ and $z = 0.656 + 3.60 \times f_{H2O}$.

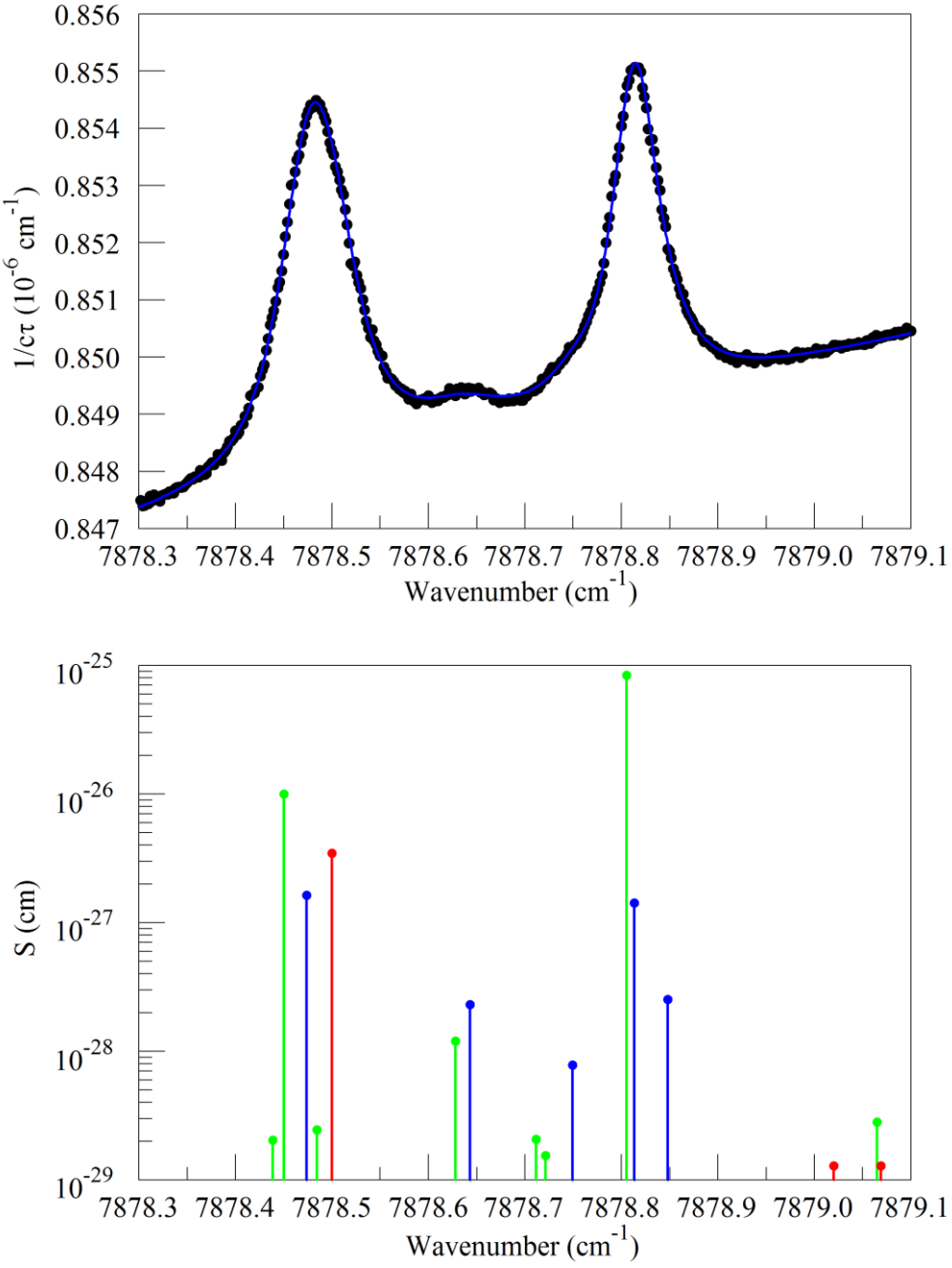

764

765 Figure 5. Upper panel: spectrum of water in nitrogen (points) and fit to Voigt model (blue
766 curve). Lower panel: Oxygen (green), normal water (blue), and deuterated water (red) lines
767 in the 2016 Hitran data base.

768

769

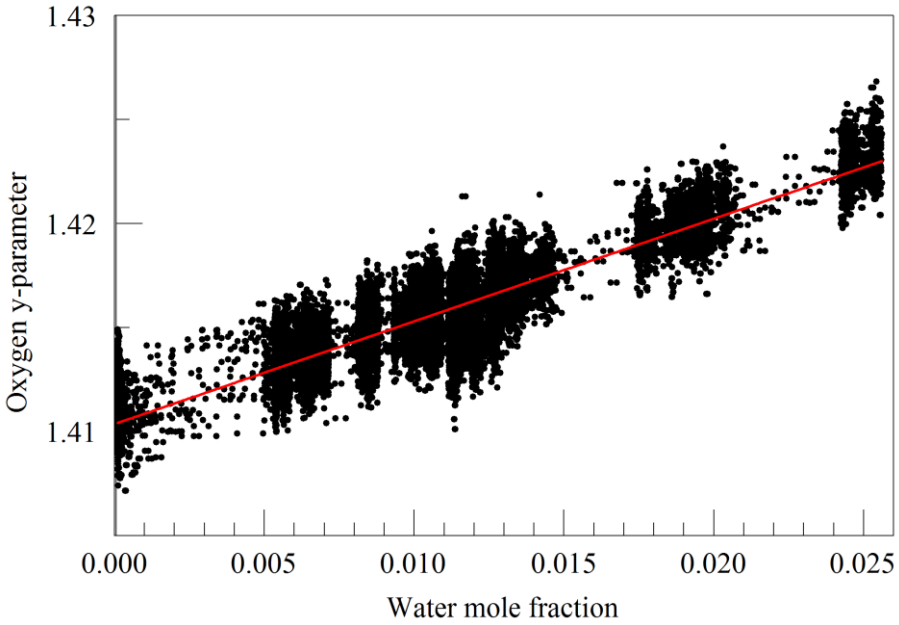

Figure 6. Galatry collisional broadening parameter of the oxygen Q13Q13 line at 340 hPa and 45° C versus water mole fraction. Black points are from measurements and the red line is a linear fit: $y = 1.4109 + 0.467\ f_{H2O}$.

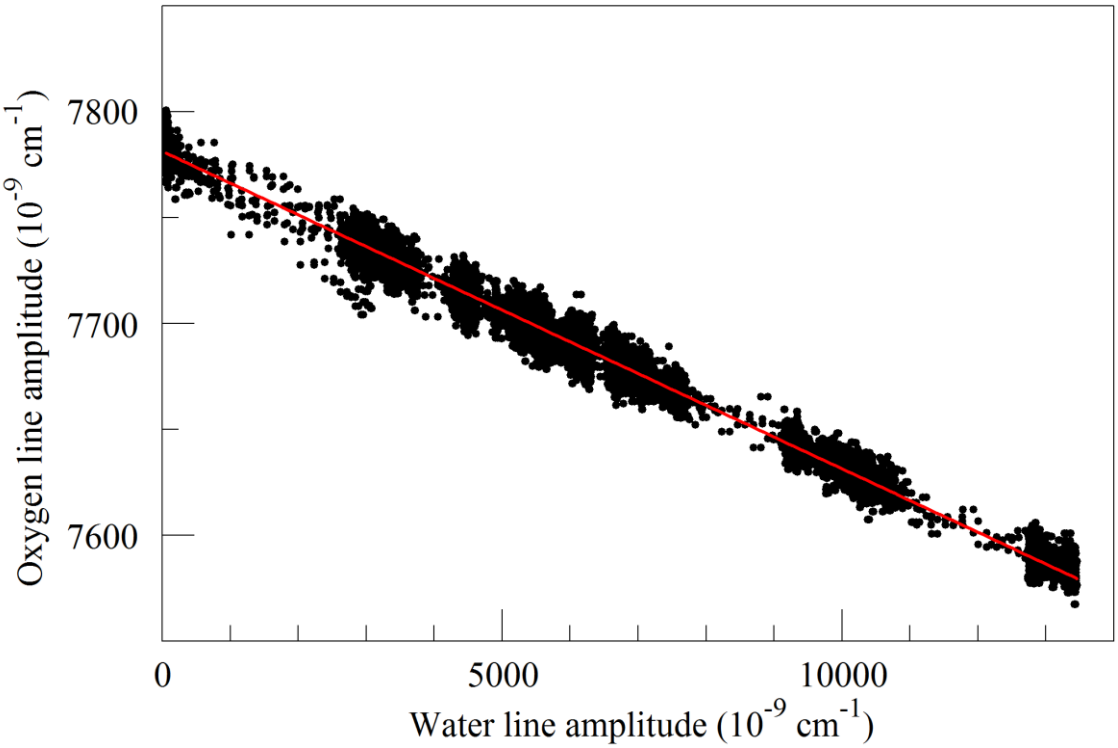

Figure 7. Measured absorption line amplitudes for oxygen and water vapor for water vapor mixing ratios ranging from nearly 0 to 0.025. Black points are from measurements and the red line is a linear fit: with intercept 7.78001 x 10^{-6} cm^{-1} and slope -0.014807.

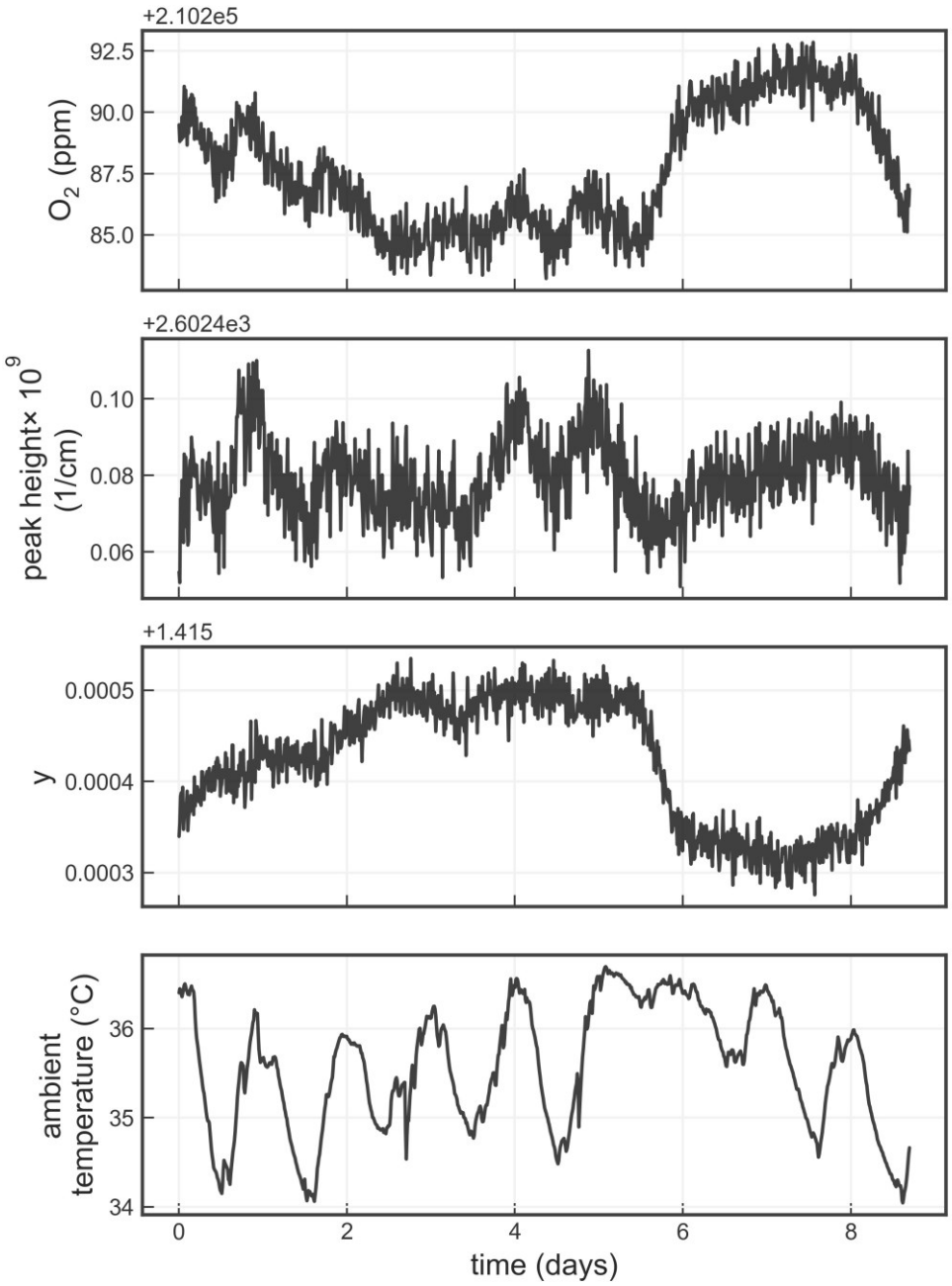

787

788 Figure 8. Time series from a measurement of a single tank over about a week. The four panels
789 show the water-corrected oxygen concentration, the absorption peak loss minus the baseline
790 loss, the measured Lorentzian broadening factor, and the ambient temperature (measured in
791 the instrument housing), respectively. A windowed average of 300 seconds was applied to all
792 four data sets.

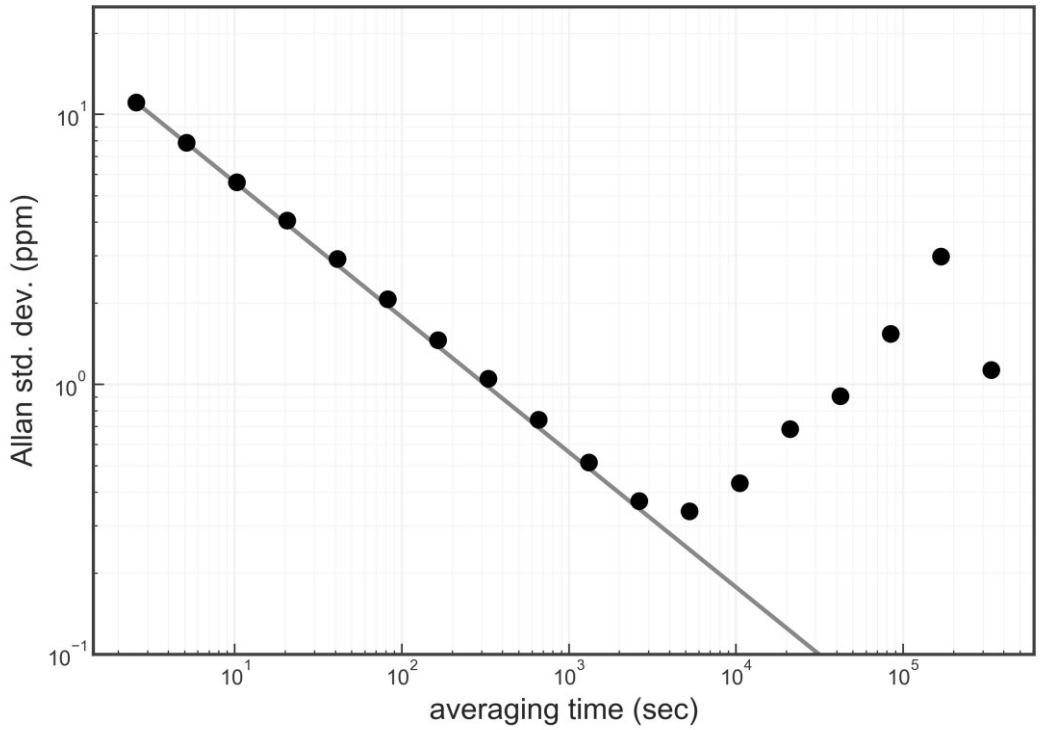

793

794 Figure 9. Precision of O_2 mole fraction measured from a tank of synthetic air. Filled circles

795 are measurements and the line shows the ideal $\tau^{-1/2}$ dependence.

796

797

798

799

800

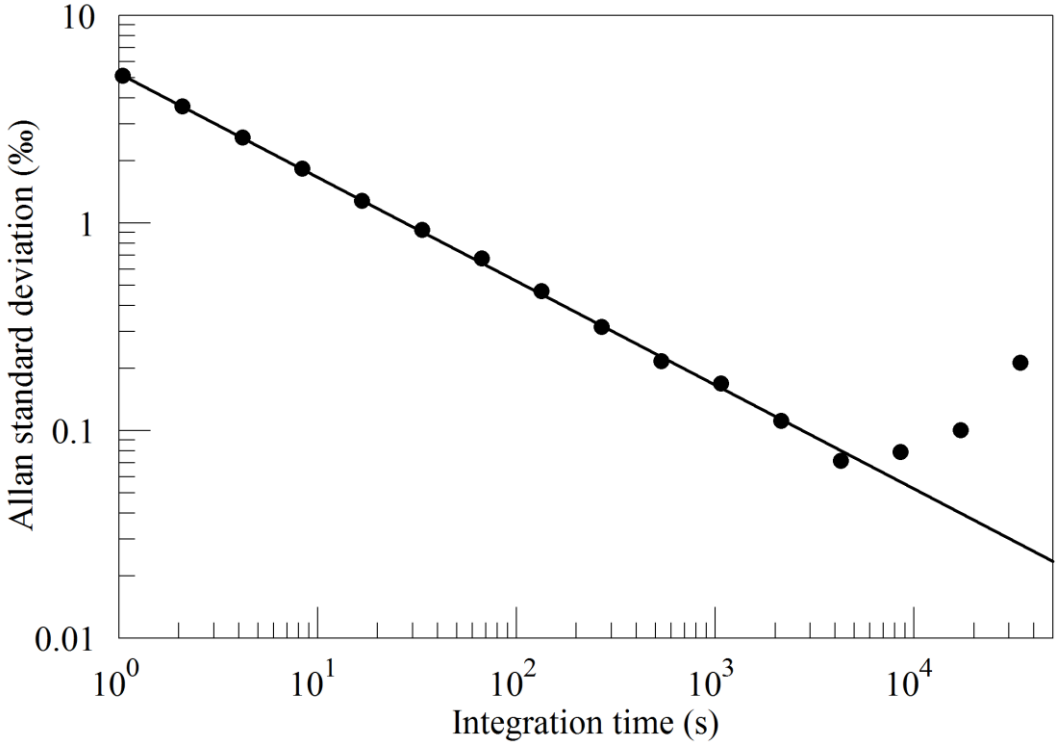

Figure 10. Precision of $\delta(^{18}O)$ measured from a tank of synthetic air. Filled circles are measurements and the line shows the ideal $\tau^{-1/2}$ dependence.

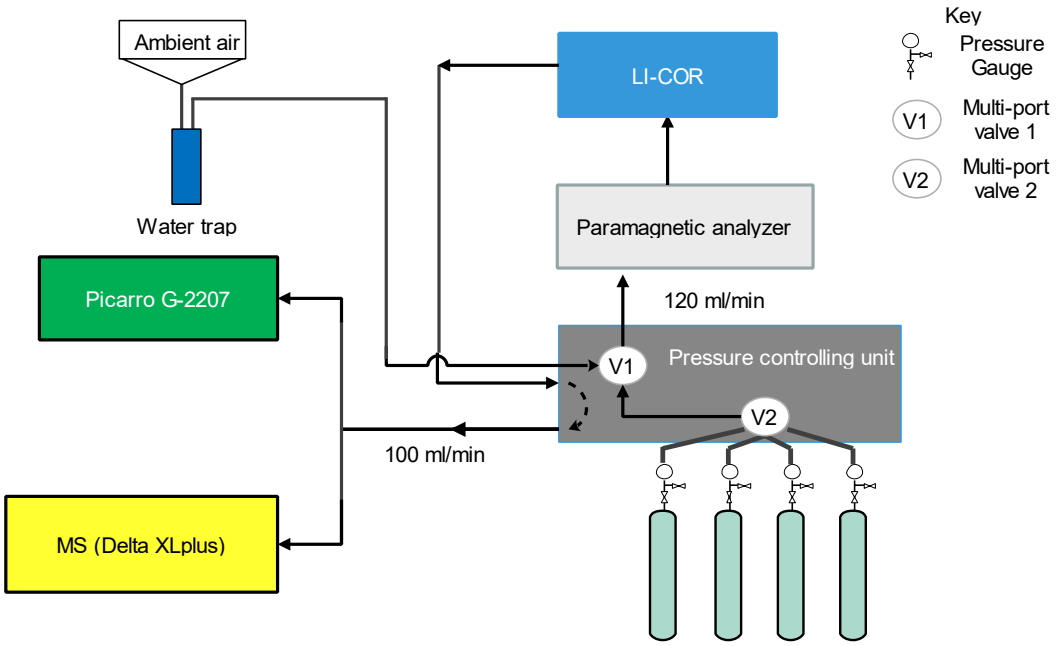

812

813 Figure 11. Schematics of the measurement system used to compare the Picarro analyzer with

814 the Mass Spectrometer at Bern.

815

816

817

818

819

820

821

822

823

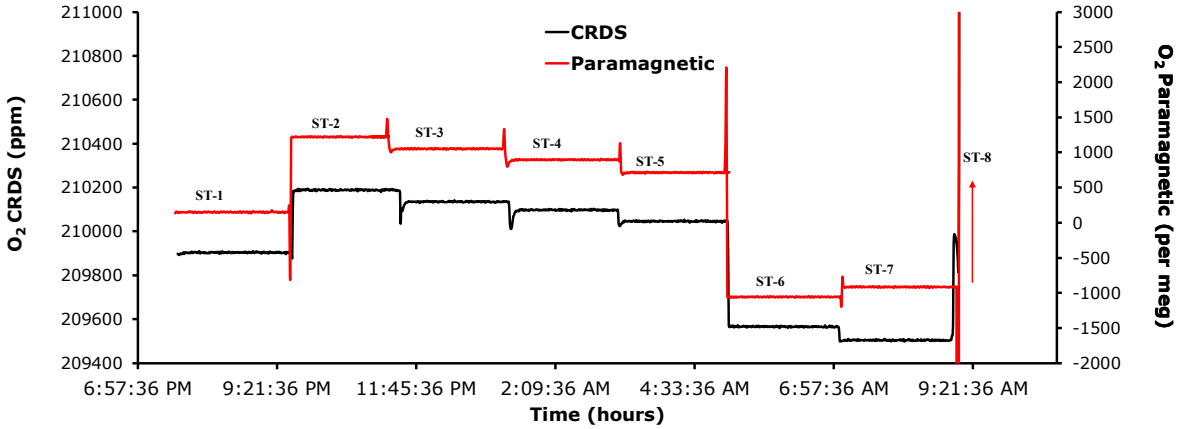

Figure 12. Comparison of oxygen mixing ratios for the seven standard gases measured using the CRDS analyzer (black) and the Paramagnetic sensors (red).

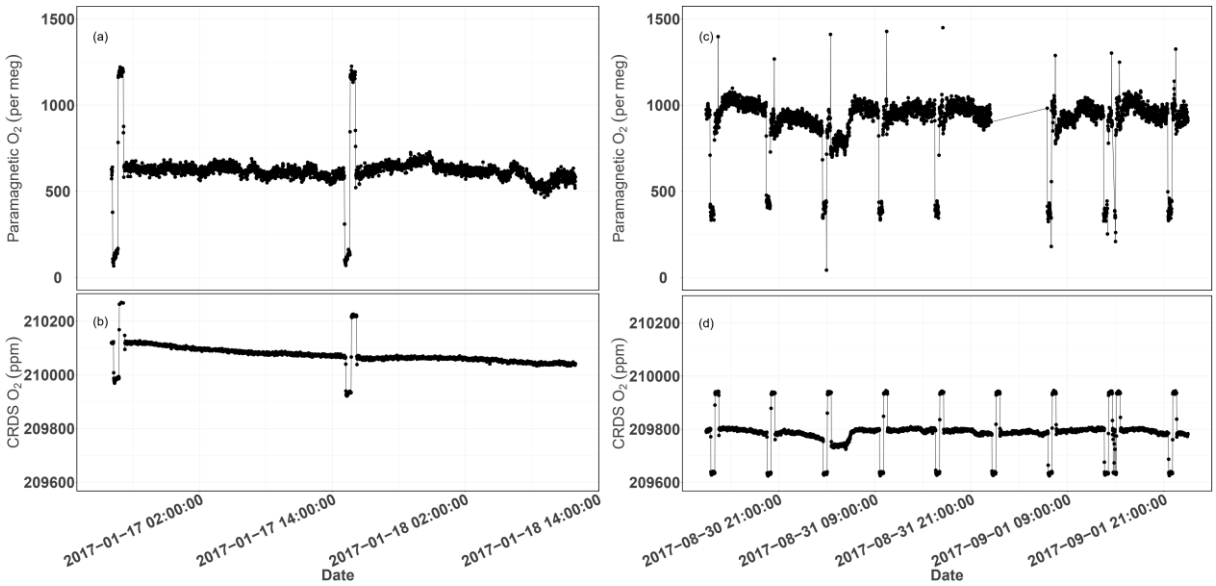

Figure 13. Parallel ambient air measurements by the Paramagnetic and CRDS analyzers at the beginning of the testing period (Panels a & b, January 2017) and the second phase of testing (Panels c & d, September 2017). The spikes are measurements from the two standard gases bracketing the ambient air values.

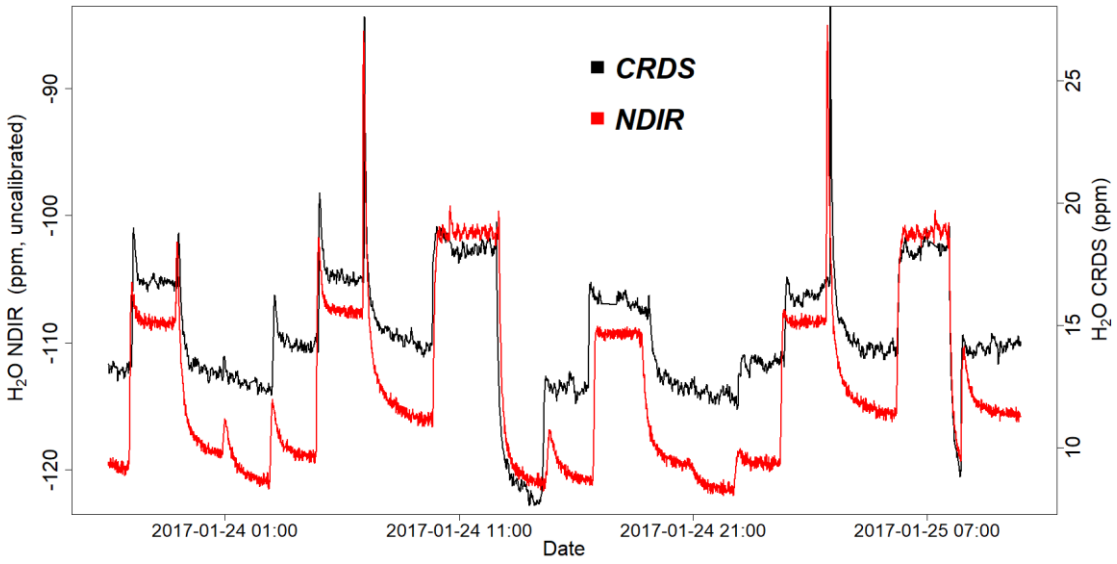

Figure 14. Parallel water vapor measurements for a dried ambient air by both the NDIR and CRDS analyzers. Note that the water values from the NDIR analyzer are not calibrated.

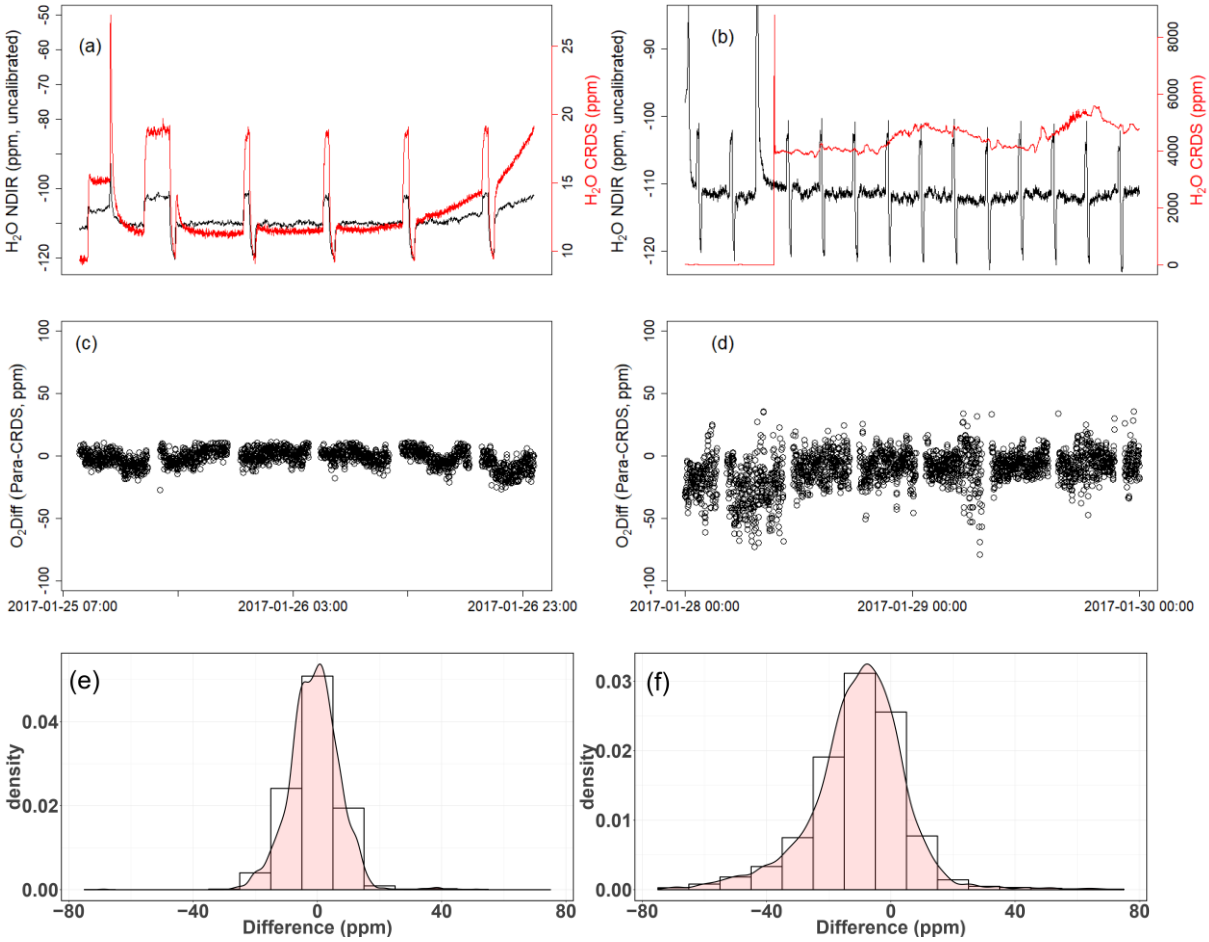

Figure 15. Results of water correction tests. Water measurements of the NDIR (left scale) for dry conditions (a,b) and the CRDS analyzer (right scale) for dry (a) and wet (b) conditions. The difference in oxygen measurements between the Paramagnetic and the CRDS instrument using the built-in water correction for the CRDS values under dry (c) and wet (d) conditions. Panels (e) and (f) show the population density functions.

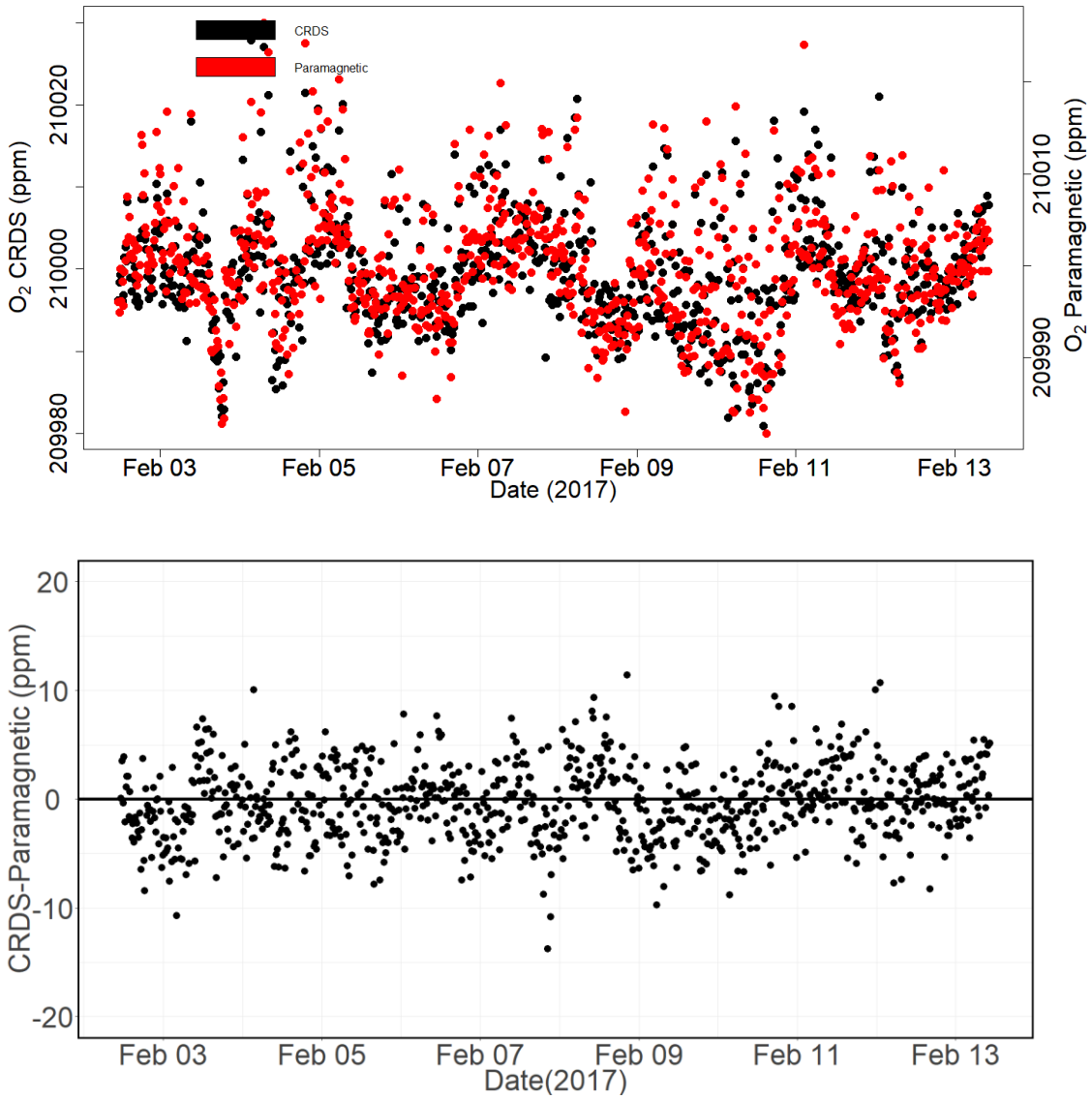

Figure 16. Calibrated ambient air oxygen measurements (1-minute average) at the Jungfraujoch site using the CRDS and Paramagnetic analyzers both in ppm units (a) and the absolute difference between the two measurements in ppm (b) by matching time stamps

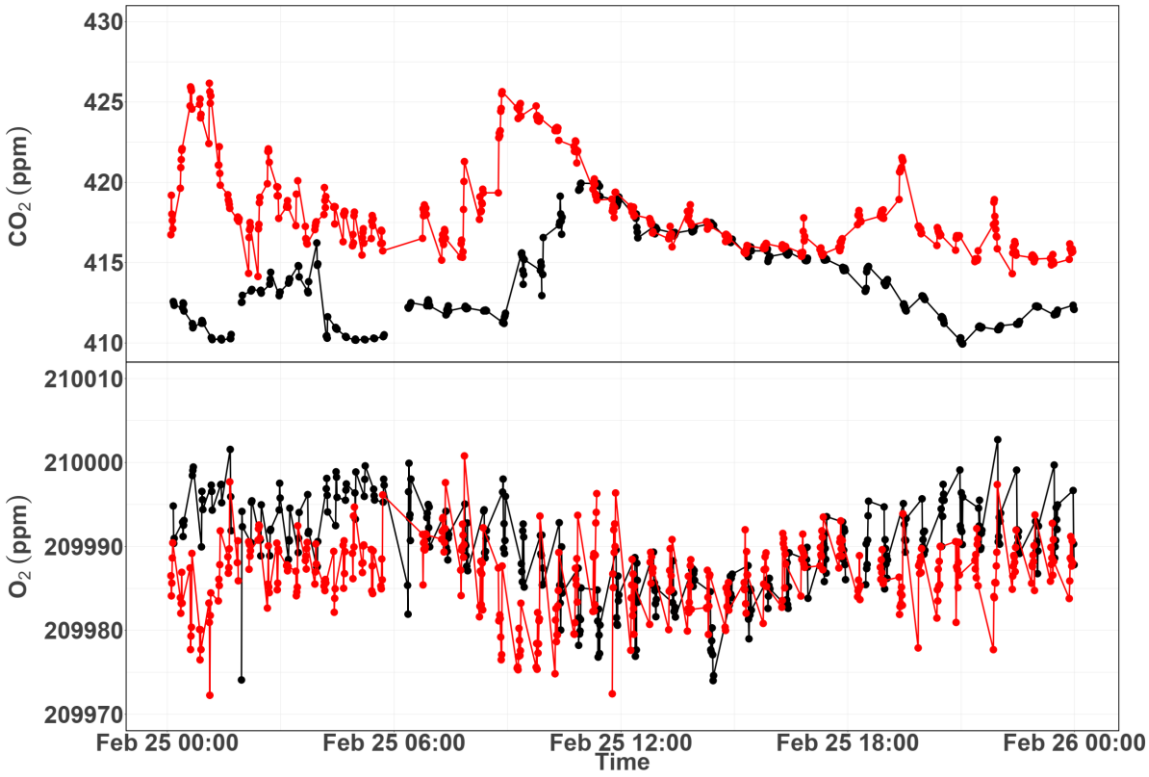

Figure 17. Diurnal variations of CO_2 (top) and O_2 (bottom) measurements from the 12 m (red) and the 212.5 m (black) height levels at Beromünster tower.

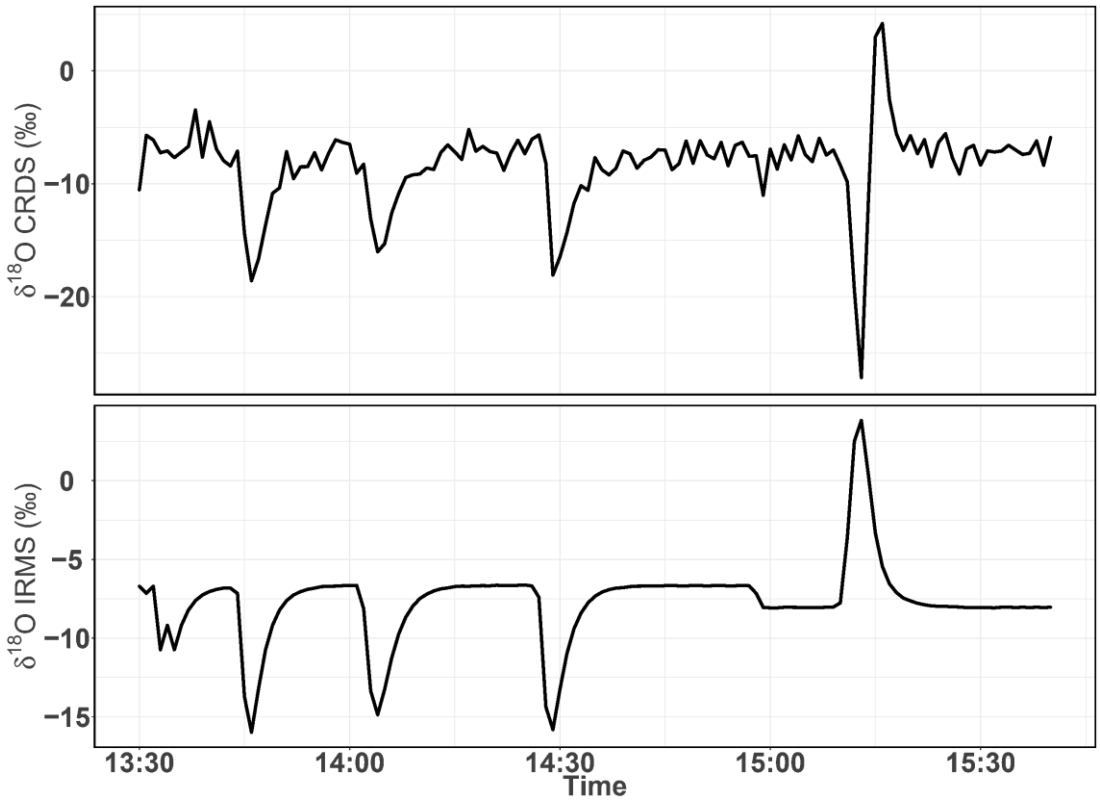

Figure 18. Consecutive $\delta^{18}O$ measurements of a standard gas (CO_2-free air) filled into three flasks followed by measurement of breath air using the CRDS analyzer (top) and IRMS (bottom). These measurements were carried out in the middle of ambient air measurements.

Appendix A.

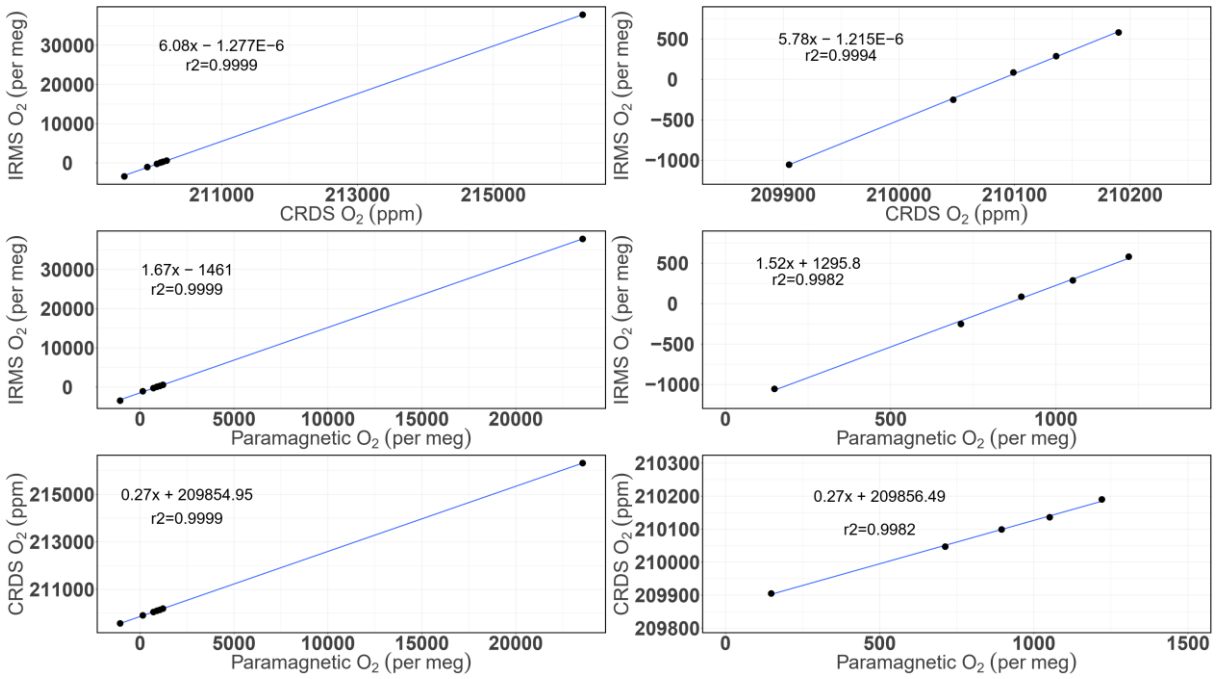

Figure A.1. Correlations between the O_2 mixing ratios measured by the CRDS and Paramagnetic analyzers with the mass spectrometric measurements (uncalibrated values). The left panels are for all the cylinders measured (standards 1 to 8) while the right ones are after selecting standards 1-5.

940 **References**

941 Battle, M., Bender, M. L., Tans, P. P., White, J. W. C., Ellis, J. T., Conway, T., and Francey, R. J.: Global
942 carbon sinks and their variability inferred from atmospheric O-2 and delta C-13, Science, 287, 2467-
943 2470, 2000.
944 Bender, M. L., Tans, P. P., Ellis, J. T., Orchardo, J., and Habfast, K.: A High-Precision Isotope Ratio
945 Mass-Spectrometry Method for Measuring the O-2 N-2 Ratio of Air, Geochim Cosmochim Ac, 58,
946 4751-4758, 1994.
947 Berhanu, T. A., Satar, E., Schanda, R., Nyfeler, P., Moret, H., Brunner, D., Oney, B., and Leuenberger,
948 M.: Measurements of greenhouse gases at Beromünster tall tower station in Switzerland, Atmos.
949 Meas. Tech. , 9, 2016.
950 Berhanu, T. A., Szidat, S., Brunner, D., Satar, E., Schanda, R., Nyfeler, P., Battaglia, M., Steinbacher,
951 M., Hammer, S., and Leuenberger, M.: Estimation of the fossil-fuel component in atmospheric CO2
952 based on radiocarbon measurements at the Beromünster tall tower, Switzerland, Atmos. Chem.
953 Phys. Discuss., 2017, 1-33, 2017.
954 Crosson, E. R. J. A. P. B.: A cavity ring-down analyzer for measuring atmospheric levels of methane,
955 carbon dioxide, and water vapor, 92, 403-408, 2008.
956 Filges, A., Gerbig, C., Rella, C. W., Hoffnagle, J., Smit, H., KrÃ¤mer, M., Spelten, N., Rolf, C., BozÃ³ki, Z.,
957 Buchholz, B., and Ebert, V.: Evaluation of the IAGOS-Core GHG Package H2O measurements during
958 the DENCHAR airborne inter-comparison campaign in 2011, Atmos. Meas. Tech., 11, 5279–5297,
959 2018, https://doi.org/10.5194/amt-11-5279-2018. Gao, F., Zhang, X., Zhang, X., Wang, M., and Wang,
960 P.: Virtual electronic nose with diagnosis model for the detection of hydrogen and methane in breath
961 from gastrointestinal bacteria, 28-31 May 2017 2017, 1-3.
962 Gordon, E., Rothman, S., Hill, C., Kochanov, V., Tan, Y., Bernath, P., Birk, M., Boudon, V., Campargue,
963 A., Chance, K., Drouin, J., Flaud, J., Gamache, R. R., Hodges, J., Jacquemart, D., Perevalov, I., Perrin, A.,
964 Shine, P., Smith, M., Tennyson, J., Toon, G., Tran, H., Tyuterev, G., Barbe, A., Császár, G., Devi, M.,

965 Furtenbacher, T., Harrison, J., Hartmann, J., Jolly, A., Johnson, J., Karman, T., Kleiner, I., Kyuberis, A.
966 A., Loos, J., Lyulin, M., Massie, S., Mikhailenko, S., Moazzen-Ahmadi, N., Muller, S., Naumenko, O. V.,
967 Nikitin, A. V., Polyansky, O. L., Rey, M., Rotger, M., Sharpe, S., Sung, K., Starikova, E., Tashkun, S.,
968 Auwera, J., Wagner, G., Wilzewski, J., Wcisło, P., Yu, S., and Zak, E. J.: The HITRAN2016 molecular
969 spectroscopic database, 203, 3 - 69, 2017.
970 Goto, D., Morimoto, S., Ishidoya, S., Aoki, S., and Nakazawa, T.: Terrestrial biospheric and oceanic
971 CO2 uptake estimated from long-term measurements of atmospheric CO2 mole fraction, δ13C and
972 δ(O2/N2) at Ny-Ålesund, Svalbard, Journal of Geophysical Research: Biogeosciences, doi:
973 10.1002/2017JG003845, 2017. n/a-n/a, 2017.
974 Gottlieb, K., Le, C. X., Wacher, V., Sliman, J., Cruz, C., Porter, T., and Carter, S.: Selection of a cut-off
975 for high- and low-methane producers using a spot-methane breath test: results from a large north
976 American dataset of hydrogen, methane and carbon dioxide measurements in breath, Gastroenterol
977 Rep, 5, 193-199, 2017.
978 Hartmann, J.-M., Boulet, C., and Robert, D.: Collisional Effects on Molecular Spectra, Elsevier Science,
979 2008.
980 Henne, S., Brunner, D., Folini, D., Solberg, S., Klausen, J., and Buchmann, B.: Assessment of
981 parameters describing representativeness of air quality in-situ measurement sites, Atmos. Chem.
982 Phys., 10, 3561-3581, 2010.
983 Hodges, J. T., Layer, H. P., Miller, W. W., and Scace, G. E.: Frequency-stabilized single-mode cavity
984 ring-down apparatus for high-resolution absorption spectroscopy, 75, 849-863, 2004.
985 Keeling, R. F.: Development of an Interferometric Oxygen Analyzer for Precise Measurement of the
986 Atmospheric O2 Mole Fraction, UMI, 1988a.
987 Keeling, R. F.: Measuring correlations between atmospheric oxygen and carbon dioxide mole
988 fractions: A preliminary study in urban air, J Atmos Chem, 7, 153-176, 1988b.

989 Keeling, R. F. and Manning, A. C.: 5.15 - Studies of Recent Changes in Atmospheric O2 Content A2 -
990 Holland, Heinrich D. In: Treatise on Geochemistry (Second Edition), Turekian, K. K. (Ed.), Elsevier,
991 Oxford, 2014.
992 Keeling, R. F. and Shertz, S. R.: Seasonal and Interannual Variations in Atmospheric Oxygen and
993 Implications for the Global Carbon-Cycle, Nature, 358, 723-727, 1992.
994 Keeling, R. F., Stephens, B. B., Najjar, R. G., Doney, S. C., Archer, D., and Heimann, M.: Seasonal
995 variations in the atmospheric O-2/N-2 ratio in relation to the kinetics of air-sea gas exchange, Global
996 Biogeochem Cy, 12, 141-163, 1998.
997 Lamouroux, J., Sironneau, V., Hodges, J. T., and Hartmann, J. M.: Isolated line shapes of molecular
998 oxygen: Requantized classical molecular dynamics calculations versus measurements, Physical
999 Review A, 89, 042504, 2014.
1000 Le Quéré, C., Andrew, R. M., Friedlingstein, P., Sitch, S., Pongratz, J., Manning, A. C., Korsbakken, J. I.,
1001 Peters, G. P., Canadell, J. G., Jackson, R. B., Boden, T. A., Tans, P. P., Andrews, O. D., Arora, V. K.,
1002 Bakker, D. C. E., Barbero, L., Becker, M., Betts, R. A., Bopp, L., Chevallier, F., Chini, L. P., Ciais, P.,
1003 Cosca, C. E., Cross, J., Currie, K., Gasser, T., Harris, I., Hauck, J., Haverd, V., Houghton, R. A., Hunt, C.
1004 W., Hurtt, G., Ilyina, T., Jain, A. K., Kato, E., Kautz, M., Keeling, R. F., Klein Goldewijk, K., Körtzinger, A.,
1005 Landschützer, P., Lefèvre, N., Lenton, A., Lienert, S., Lima, I., Lombardozzi, D., Metzl, N., Millero, F.,
1006 Monteiro, P. M. S., Munro, D. R., Nabel, J. E. M. S., Nakaoka, S. I., Nojiri, Y., Padín, X. A., Peregon, A.,
1007 Pfeil, B., Pierrot, D., Poulter, B., Rehder, G., Reimer, J., Rödenbeck, C., Schwinger, J., Séférian, R.,
1008 Skjelvan, I., Stocker, B. D., Tian, H., Tilbrook, B., van der Laan-Luijkx, I. T., van der Werf, G. R., van
1009 Heuven, S., Viovy, N., Vuichard, N., Walker, A. P., Watson, A. J., Wiltshire, A. J., Zaehle, S., and Zhu,
1010 D.: Global Carbon Budget 2017, Earth Syst. Sci. Data Discuss., 2017, 1-79, 2017.
1011 Machta, L. and Hughes, E.: Atmo~~p~~spheric Oxygen in 1967 to 1970, Science, 168, 3939, 1582-1584,
1012 1970.

1013 Manning, A.: Temporal variability of atmospheric oxygen from both continuos and measurements
1014 and a flask sampling network: tools for studying the global carbon cycle, Ph.D. Ph.D., University of
1015 California, San Diego, San Diego, Calofornia, USA, 2001.
1016 Manning, A. C. and Keeling, R. F.: Global oceanic and land biotic carbon sinks from the Scripps
1017 atmospheric oxygen flask sampling network, Tellus B, 58, 95-116, 2006.
1018 Manning, A. C., Keeling, R. F., and Severinghaus, J. P.: Precise atmospheric oxygen measurements
1019 with a paramagnetic oxygen analyzer, Global Biogeochem Cy, 13, 1107-1115, 1999.
1020 Marrero, T. R. and Mason, E. A.: Gaseous Diffusion Coefficients, Journal of Physical and Chemical
1021 Reference Data 1, 3, 1972.
1022 Martin, N. A., Ferracci, V., Cassidy, N., and Hoffnagle, J. A. J. A. P. B.: The application of a cavity ring-
1023 down spectrometer to measurements of ambient ammonia using traceable primary standard gas
1024 mixtures, 122, 219, 2016.
1025 Mckay, L. F., Eastwood, M. A., and Brydon, W. G.: Methane Excretion in Man - a Study of Breath,
1026 Flatus, and Feces, Gut, 26, 69-74, 1985.
1027 Nevison, C. D., Keeling, R. F., Kahru, M., Manizza, M., Mitchell, B. G., and Cassar, N.: Estimating net
1028 community production in the Southern Ocean based on atmospheric potential oxygen and satellite
1029 ocean color data, Global Biogeochem Cy, 26, 2012.
1030 Oney, B., Henne, S., Gruber, N., Leuenberger, M., Bamberger, I., Eugster, W., and Brunner, D.: The
1031 CarboCount CH sites: characterization of a dense greenhouse gas observation network, Atmos.
1032 Chem. Phys., 15, 11147-11164, 2015.
1033 Press, W. H., Teukolsky, S. A., Vetterling, W. T., and Flannery, B. P.: Numerical Recipes 3rd Edition:
1034 The Art of Scientific Computing, Cambridge Printing Press, Cambridge, England, 1986.
1035 Press, W. H., Teukolsky, S. A., Vetterling, W. T., and Flannery, B. P.: Numerical recipes in C: the art of
1036 scientific computing, Cambridge University Press, London, 1992.

1037 Ryter, S. W. and Choi, A. M. K.: Carbon monoxide in exhaled breath testing and therapeutics, J Breath
1038 Res, 7, 2013.
1039 Satar, E., Berhanu, T. A., Brunner, D., Henne, S., and Leuenberger, M.: Continuous CO2/CH4/CO
1040 measurements (2012–2014) at Beromünster tall tower station in Switzerland, Biogeosciences, 13,
1041 2623-2635, 2016.
1042 Schibig, M. F., Steinbacher, M., Buchmann, B., van der Laan-Luijkx, I. T., van der Laan, S., Ranjan, S.
1043 and Leuenberger, M. C,: Comparison of continuous in situ CO2 observations at Jungfraujoch using
1044 two different measurement techniques, Atmospheric Measurement Techniques
1045 , 8, 57-68, 10.5194/amt-8-57-2015, 2015.
1046 Severinghaus, J. P.: Studies of the terresterial O2 and carbon cycles in sand dune gases and in
1047 Biosphere Doctoral Ph.D., Columbia University, New York, USA, 1995.
1048 Steig, E. J., Gkinis, V., Schauer, A. J., Schoenemann, S. W., Samek, K., Hoffnagle, J., Dennis, K. J., and
1049 Tan, S. M.: Calibrated high-precision ¹⁷O-excess measurements using cavity ring-down
1050 spectroscopy with laser-current-tuned cavity resonance, Atmos. Meas. Tech., 7, 2014.
1051 Stephens, B. B., Bakwin, P. S., Tans, P. P., Teclaw, R. M., and Baumann, D. D.: Application of a
1052 differential fuel-cell analyzer for measuring atmospheric oxygen variations, J Atmos Ocean Tech, 24,
1053 82-94, 2007.
1054 Sturm, P., Leuenberger, M., Valentino, F.L., Lehmann, B. and B. Ihly: Measurements of CO_2, its stable
1055 isotopes, O_2/N_2, and ^{222}Rn at Bern, Switzerland, *Atmospheric Chemistry and Physics*, *6*, 1991-2004,
1056 2006.

1057 Tan, Y., Kochanov, R.V., Rothman, L., and Gordon, I.E.:Introduction of water-vapor broadening
1058 coefficients and their temeprature dependence exponents into the HITRAN database, Part 1: CO2,
1059 N2O, CO, CH4, O2, NH3, and H2S, Submitted to Journal of Geophysical Research Atmospheres, 2019,
1060 arXiv:1906.01475 .

1061 Tennyson, J., Bernath, P. F., Campargue, A., Császár, A. G., Daumont, L., Gamache, R. R., Hodges, J. T.,
1062 Lisak, D., Naumenko, O. V., Rothman, L. S., Tran, H., Zobov, N. F., Buldyreva, J., Boone, C. D., De Vizia,
1063 M. D., Gianfrani, L., Hartmann, J.-M., McPheat, R., Weidmann, D., Murray, J., Ngo, N. H., and
1064 Polyansky, O. L.: Recommended isolated-line profile for representing high-resolution spectroscopic
1065 transitions (IUPAC Technical Report), 86, 1931–1943, 2014.
1066 Tohjima, Y.: Method for measuring changes in the atmospheric O-2/N-2 ratio by a gas
1067 chromatograph equipped with a thermal conductivity detector, J Geophys Res-Atmos, 105, 14575-
1068 14584, 2000.
1069 Tran, H., Turbet, M., Hanoufa, S., Landsheere, X., Chelin, P., Ma, Q., Hartmann, J.: The CO2–
1070 broadened H2O continuum in the 100–1500 cm-1 region: Measurements, predictions and empirical
1071 model, Journal of Quantitative Spectroscopy and Radiative Transfer, 230, 75-80, 2019.
1072 Valentino, F. L., Leuenberger, M., Uglietti, C., and Sturm, P.: Measurements and trend analysis of O2,
1073 CO2 and δ13C of CO2 from the high altitude research station Junfgraujoch, Switzerland — A
1074 comparison with the observations from the remote site Puy de Dôme, France, Sci Total Environ, 391,
1075 203-210, 2008.
1076 Varghese, P. L. and Hanson, R. K.: Collisional narrowing effects on spectral line shapes measured at
1077 high resolution, Appl. Opt., 23, 2376-2385, 1984.
1078 Wójtewicz, S., Cygan, A., Masłowski, P., Domysławska, J., Wcisło, P., Zaborowski, M., Lisak, D.,
1079 Trawiński, R. S., and Ciuryło, R.: Spectral line-shapes of oxygen B-band transitions measured with
1080 cavity ring-down spectroscopy, Journal of Physics: Conference Series, 548, 012028, 2014.
1081 Wolf, P. G., Parthasarathy, G., Chen, J., O'Connor, H. M., Chia, N., Bharucha, A. E., and Gaskins, H. R.:
1082 Assessing the colonic microbiome, hydrogenogenic and hydrogenotrophic genes, transit and breath
1083 methane in constipation, Neurogastroent Motil, 29, 2017.

1084 Zellweger, C., Forrer, J., Hofer, P., Nyeki, S., Schwarzenbach, B., Weingartner, E., Ammann, M., and
1085 Baltensperger, U.: Partitioning of reactive nitrogen (NO_y) and dependence on
1086 meteorological conditions in the lower free troposphere, Atmos. Chem. Phys., 3, 779-796, 2003.

1087